DUAL-POLARIZATION MULTI-FREQUENCY RADAR DATA PROCESSING FOR MOVING TARGET DETECTION

DUAL-POLARIZATION MULTI-FREQUENCY RADAR DATA PROCESSING FOR MOVING TARGET DETECTION

DISSERTATION

to obtain the degree of Master of Science
in Electrical Engineering
at Delft University of Technology,
to be defended publicly on 15th November, 2021 at 10:30 AM

by

Huaiyang GONG

born in Liaoning, China.

This thesis has been approved by the

supervisor: Prof. Dsc. Alexander Yarovoy
daily supervisor: Dr. Nikita Petrov

Thesis committee:

Prof. Dsc. Alexander Yarovoy	MS3 TU Delft
Prof. dr. A. Richard Hendriks	CAS TU Delft
Dr. Nikita Petrov	MS3 TU Delft

ACKNOWLEDGEMENTS

I think I would not regret the decision I made two years ago to study at TU Delft. The knowledge I learned in the past two years, so many kind people I met, the process of falling and rising, frustrated and proud, all of these will become very precious memories in later life. At the end of this remarkable journey of Master's study, I want to express my sincerest gratitude to the people who have accompanied and helped me during this period.

Firstly, I would like to thank the guidance of my supervisor, **Prof. DSc. Alexander Yarovoy**, for giving me a lot of helpful advice and encouragement. Even though he has a hectic schedule, he still pays attention to my progress every month and offers valuable suggestions. When I was at a loss in the initial stage of the project, he encouraged me with his gentleness and patience, which gave me the courage to persevere, and more and more discover the exciting aspects of scientific research.

I am very grateful to my daily supervisor, **Dr. Nikita Petrov**, for his patient guidance and company over the past nine months. Without him, I can't imagine that I would be where I am today. Whenever I encounter a problem, he can always give me instrumental help in time. The knowledge he taught me during this time will be helpful for my future study.

I am sincerely grateful to my best friend, Jiaxuan Ren. Even though she is thousands of miles away, she still warms me with her best enthusiasm, patience, and company. She can always pull me out of the dilemma when I am in negative emotions and help me regain the strength and confidence to persevere. Specially thanks to my friends Ying Zhang, Yi Mi, and Yichuang Han, for accompanying me in this difficult Covid-19 period.

Finally, my most solemn gratitude is left to my parents. They always say that they will be my most robust backing. Whether I am successful or not, whether I want to go to the outside world or return to my hometown, they will always support me, encourage me, and feel happy for my little progress from the bottom of their heart. They not only gave me life but also taught me courage and love. They are my warmest and safest harbor.

Huaiyang Gong
Delft, November 2021

CONTENTS

List of Figures

LIST OF TABLES

1

INTRODUCTION

1.1. MOTIVATION

The critical role of radar is to detect the object and return the speed and distance information of the target. Detection of small and maneuvering targets like drones in a cluttered environment remains challenging even for modern radars.

Typical targets of interest (cars, drones, gliders, etc.) have dimensions more significant than the wavelength of the radar (from few cm to a few meters), which implies that Radar Cross-Section (RCS) of real targets has significant and rapid variations with the aspect angle of the radar operates in a narrow band [22]. The majority of the currently operating radars work at a single frequency band, and thus the target can be missed due to being observed at the low RCS zone. Moreover, modern radars tend to use higher frequencies, which leads to the decrease of unambiguous range and velocity intervals. Therefore, these radars must deal with range-Doppler ambiguities. Typically, Doppler ambiguities are preferred. The maximum unambiguous velocity is related to the radar's wavelength and Pulse Repetition Interval (PRI). Classical radars transmit a few bursts with different PRF to resolve them. The range ambiguities can occur in the scenario of detecting a weak target at far range against the strong clutter from nearby.

However, in the case of multi-frequency radar, the ambiguity could be resolved by taking advantage of the two radar's different carrier frequencies [12]; and the polarimetric diversity of radar could give a complete description of the target in different directions [22]. Therefore, data fusion methods with frequency and polarimetric diversity are foreseen to improve radar performance under challenging scenarios. Such systems will benefit from the frequency and polarimetry diversity gained from the joint processing of multiple independent channels. This diversity gives a complete description of the target, which will also improve the potential of the target from clutter discrimination and classification.

1

1.2. HARDWARE DESCRIPTION

Some basic information about the two radars is listed here. The PARSAX radar, which operates at S-band, has a central frequency 3.315 GHz [21]. The MESEWI radar is an X-band polarimetric Doppler scanning radar operating at around 9.6 GHz. They are both fully polarimetric, which means they all have two independent, highly linear polarimetric RF channels in the transmitter and receiver.

The two radars have a flexible range and Doppler resolution. The beam-width of their antennas is of the same order of magnitude (1.8 degree) [31, 48]. Thus the primary source of diversity in their data is the different operational frequency. Fusing the data from the two radars, using the diversity of polarization and frequency could improve the performance of target detection and feature extraction.

However, since the two radars operate independently and have different hardware (including the delay lines), they slightly differ in timing synchronized by GPS (1 stamp per second) / PC time. Moreover, they a located a few meters away from each other, which will lead to the difference in their range measurements, especially in meter range resolution.

1.3. GOALS

Algorithms for joint signal processing of data from two radars located on the rooftop of EWI (PARSAX and MESEWI) will be developed and tested in this project. The particular tasks consist of automatic alignment of radar data in space (2D map) and time (with sub-second accuracy, using Global Positioning System(GPS) / Personal Computer(PC) timestamps for initialization) by observing moving targets of opportunity in the high-resolution mode. After the data alignment procedure, the detection algorithms for optimal fusing of dual-polarization and multi-frequency data will be developed. The alignment procedure, data fusion and detection algorithms will be verified with experimental data.

1.4. LITERATURE REVIEW

Data alignment is the pre-processing procedure for joint radar processing of measurements from different radars [16]. For spatial alignment, some valuable methods have been developed in this field, including the least-square process [52], used when the position of the target is known before spatial alignment, and online methods such as Extended Kalman Filter(EKF), Unscented Kalman Filter(UKF), or Cubature Kalman Filter(CKF) based, used when the position of the target is unknown[16]. Some temporal alignment methods have been proposed up to now, e.g., Dynamic Time Warping (DTW) [40], Hidden Markov Models(HMM), Recurrent Neural Networks(RNN) or Action Spectogram [45, 25, 29]. The proposed alignment method in this project in the two domains is based on using cross-correlation theory [27] to find the offset between data, which is easier and more efficient to understand and use.

In the data fusion part, many types of research were developed in the polarimetric radar detection area [6, 35]. Some well-known detectors were used for fusing the data from different polarized channels of a single radar. The span detector [9] is widely used because it simply takes the non-coherent sum of all polarimetric channels per-

forms better than an individual channel. Nevertheless, when the background contains complex clutter, the threshold is difficult to compute; this limits the application of this detector. Then an extension of it was designed as Power Maximization Synthesis(PMS) detector [6]. When one has exact information of the target a clutter covariances and the target to clutter ratio, Optimal Polarimetric Detector(OPD) could have improved performance [35] than a single channel. Identity-Likelihood-Ratio-Test(ILRT) detector [11] was proposed by DeGraff as an alternative to OPD. Polarimetric Whitening Filter(PWF) [34], which is also widely used in this field, has been proved to minimize the standard deviation-to-mean ratio of the clutter background in a SAR image [9].

When coming to the multi-frequency data fusion field, one popular method is using wavelet transform [26, 28]; it can give a good signal-to-noise ratio compared to pixel-based approaches and reserve more spatial features. The Principal-component transform, which was proposed by Singh and Harrison [46], could fuse images with high spatial quality, extract main features to minimize redundancy and keep a better resolution. Most of the data fusion methods in multi-frequency areas are related to image fusion; some popular methods like the Laplacian Pyramid (LP) fusion [18, 7], which decomposes the original image into sub-images with different spatial resolutions; the high-resolution sub-images are placed at the bottom, and the low-resolution sub-images are placed on top to form Pyramid. The disadvantage of this method is that it could cause a computation burden. Automatic fusion procedure [26] can provide convenience for Ground Penetrating Radar(GPR) users directly and reduce the workload of data analysis. However, it is challenging to keep the smoothness of the composite profile when it goes from high-frequency to low-frequency slices if the pre-fusion profiles are significantly different.

When we talk about multi-channel target tracking, most researchers treat this problem as multiple measurement target tracking. Typical multiple measurement tracking methods like probability associated filter [4] merge the hypothesis from each measurement. The study [13] compared two methods used for Kalman filter-based multi-sensor data fusion. The first method merges the multi-sensor data through the observation vector of the Kalman filter, whereas the second one combines the multi-sensor data based on a minimum-mean-square-error criterion. In the other research [1], the State Vector Fusion (SVF), Measurement Fusion (MF) and Gain fusion (GF) are implemented in the tracking system. These all are valuable methods in this field. However, most of these methods are developed to avoid miss detection and false alarms. If the ambiguities are resolved adequately after detection, a simple Kalman filter can perform target tracking.

1.5. NOVELTIES AND CONTRIBUTIONS

According to the literature review, there are many types of research on fusing the dual-polarized data from different channels of one radar or fusing multi-frequency data from different sensors, respectively. However, there is a gap in doing joint processing by taking advantage of frequency and polarization diversity together. The approach addressed in this thesis aim at filling this gap, which is the novelty of this project.

The main contributions of this thesis are listed below:

- Spatial alignment between two radars is addressed using the cross-correlation method

proposed in [27]. The cable length of PARSAX and the position displacement of the two radars are estimated using this method. The approach was tested with numerical simulation and experimental data.

- The time shift between two radars was estimated using the target of opportunity. It is demonstrated that the cross-correlation method allows achieving 0.01-second accuracy in this parameter, which is significantly better than the accuracy of GPS/PC time used in the current systems.

- A logic rule for combining the data from different polarimetric and frequency channels is proposed to improve the detection performance of a multi-frequency dual-polarimetric radar system and resolve the velocity ambiguity. The rule was applied to the data, which is unfolded in velocity with the right ambiguity number.

- Target tracking for multi-frequency dual-polarimetric radar system is proposed; it exploits the logical output of the range/velocity target measurements. The applicability of the method is validated with real data.

- Range signatures of a few targets have been extracted. The measured signatures of the targets can be further used for targets classification.

1.6. THESIS STRUCTURE

The rest of the thesis is structured as follows: spatial and temporal alignment procedures using the cross-correlation method are explained and implemented in chapter 2 and 3. Chapter 4 proposes a logic rule that fuses the data from different radars to resolve ambiguities. Target tracking and range feature extraction are addressed in chapter 5, while chapter 6 concludes the thesis.

2

SPATIAL ALIGNMENT

To improve the accuracy of further processing, we should first align the two radars' data in both spatial and temporal domains. This chapter introduces a method to estimate the position displacement of the two radars and the difference of their range measurements due to the cables between the antenna and the receiver. The estimated parameters are further used to perform spatial data alignment.

2.1. INTRODUCTION

The spatial alignment is the pre-processing procedure for joint radar processing of measurements from different radars [16]. Some valuable methods include the least-squares estimation [52], used for static measurements and Extended Kalman Filter(EKF), Unscented Kalman Filter(UKF), or Cubature Kalman Filter(CKF) used for dynamic systems were proposed in this field[16]. In this project, we have two independent radars located on the rooftop of the EWI building on the TU Delft campus. Because of the position displacement and the cable length in the radar system, the two radars' PPI images would be slightly different, and the position of the same target could have different positions on the two PPI images, which may cause difficulties for subsequent data processing; this contributes to the essential role of data alignment in the joint processing procedure.

2.2. PROBLEM STATEMENT

The two radars are independent of each other, and there is no delay line information in the spatial domain. Therefore, aligning the two radars' data in a standard coordinate is essential for the following data fusion.

The two radars on Google map and a simple schematic diagram of the location of the two radars are shown in figure 2.1, where the upper of the figure represents North. The red rectangular pattern represents the rooftop of the EWI building; the blue triangular pattern indicates the position of the PARSAX, the green star is the position of MESEWI. The circles represent the scanning area of the two radars, respectively.

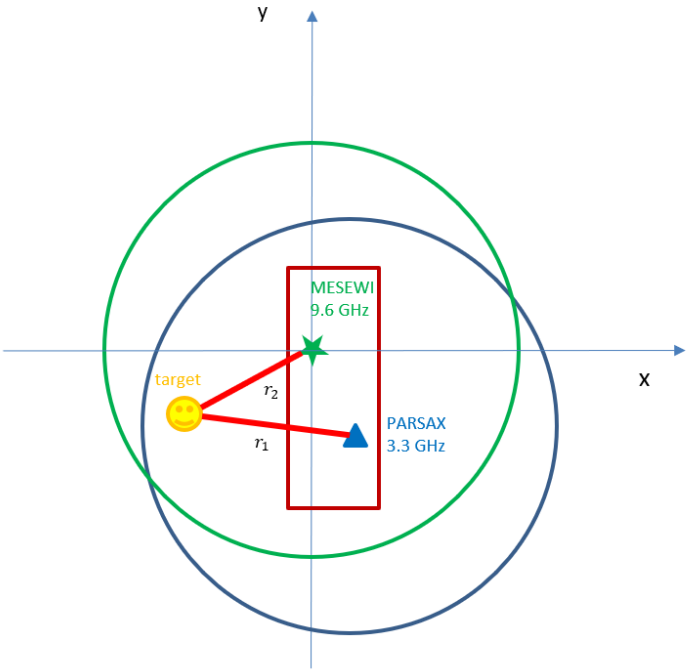

(a) Schematic diagram of the two radars

(b) Two radars on Google map

Figure 2.1: The location of the two radars

Assume that MESEWI is located in the coordinate system center, and PARSAX has a position displacement Δx and Δy. The x-axis is aligned with the local latitude, and the y axis is aligned with the meridian. For a point-like target illuminated by two radars, the distances between each radar and the target are measured, i.e., r_P for PARSAX and r_M for MESEWI. They can be calculated by

$$\begin{aligned} r_M &= \sqrt{x^2 + y^2} \\ r_P &= \sqrt{(x - \Delta x)^2 + (y - \Delta y)^2} + L_c, \end{aligned} \tag{2.1}$$

Where L_c is the cable length of PARSAX (due to system configuration, it is assumed that MESEWI has negligible cable length).

The objective of this chapter is to find a way to estimate the unknown parameters: the cable length L_c of PARSAX and the position displacement between the two radars Δx and Δy.

2.3. PROPOSED SPATIAL ALIGNMENT METHOD

Several assumptions of the two radars should be stressed below before explaining the procedure of spatial alignment.

- Two radars are located in the vicinity of each other.
- They illuminate areas at the same elevation angle.
- Each radar provides an accurate measurement of the pointing angle (azimuth and elevation).
- One radar has negligible cable length (MESEWI). Otherwise, the estimated cable length corresponds to the difference of this parameter in the two radars.

The concept of using cross-correlation to measure changes in data sets has been known and applied to digital images since at least the early 1970s [2, 17]. Digital image correlation(DIC) [27] is a commonly used method, which relies on finding the maximum of the correlation array between pixel intensity array subsets on two or more corresponding images and giving the shift value in both dimensions. After pre-processing, the data of each radar is a 2d matrix in polar coordinates, where the first dimension is the distance range between the radar and the target, the second dimension is the scanning angle. The cable length is a supplementary structure added to radar hardware, which would cause a delay in the circle center of the radar scanning image(See figure 2.2(b)). In the center of 2.2(b), there is a a small circle only contains the noise caused by the cable. In reality, since these range cells will be subject to direct Tx-RX leakage of FMCW radar, there will be interference there with no helpful information, and therefore these range cells are typically removed from the data processing.

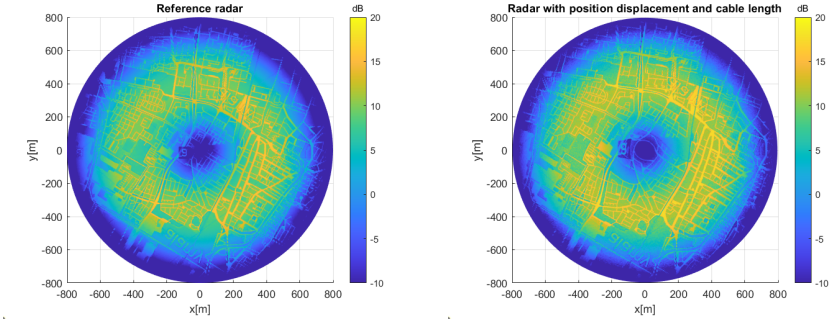

(a) Original radar scanning image

(b) Radar image with cable length

Figure 2.2: The comparison of radar images with and without cable length

Since the cable length is in polar coordinates, and the position displacement is in Cartesian coordinates, we can first use the theory of DIC to do cross-correlation in polar coordinates for estimating the cable length and then interpolate the data set to Cartesian coordinate for estimating the position displacement.

Using the theory of DIC, the cable length of PARSAX can be estimated via:

$$\hat{L}_c = \underset{r}{\operatorname{argmax}} \sum_{i=1}^{k} \sum_{j=1}^{k} (\mathbf{P}_p(\theta_i^P, r_j^P) \otimes \mathbf{P}_m(\theta_{k-i}^M, r_{k-j}^M)) \tag{2.2}$$

Where $\hat{L}_c$ represents the estimated cable length, operator $\otimes$ is the two-dimensional convolution. The matrix $\mathbf{P}_p$ and $\mathbf{P}_m$ represent the image of PARSAX and MESEWI in polar coordinates, θ_i^P is the i-th azimuth angle cell of PARSAX and r_j^P is the j-th range cell of PARSAX, the θ_i^M and r_j^M are the angle and range for MESEWI. Therefore, the shift in the range is the length of the cable, and we can get the result by doing cross-correlation of the data in polar coordinates.

There is one thing that needs to be emphasized. If the angle grid steps or the range grid steps for the two radars are different, the data of the two radars should first be interpolated to the exact radar grid and then done cross-correlation on the interpolated data.

The position displacement is in Cartesian coordinates, so the data should be interpolated to Cartesian coordinates using equation 2.3. The Matlab function 'pol2car' was used to do this implementation.

$$\begin{aligned} x &= r cos(\theta) \\ y &= r sin(\theta) \end{aligned} \tag{2.3}$$

Then using the theory of DIC in Cartesian coordinates, the displacement of the two plots can be expressed as

$$[\hat{\delta x}, \hat{\delta y}] = \underset{x,y}{\operatorname{argmax}} \sum_{i=1}^{k} \sum_{j=1}^{k} (\mathbf{C}_p(x_i^P, y_j^P) \otimes \mathbf{C}_m(x_{k-i}^M, y_{k-j}^M)) \tag{2.4}$$

Where $\hat{\delta x}, \hat{\delta y}$ represent the estimated displacement in the x and y directions. Matrix $\mathbf{C}_P$ and $\mathbf{C}_M$ represent the data of PARSAX and MESEWI in Cartesian coordinates, x_i^P is the i-th cell in x axis of PARSAX and y_j^P is the j-th cell in y axis of PARSAX, the x_i^M and y_j^M are the x and y position for MESEWI. The method in [15] was used to avoid the influence of the number of samples on the result, which selects two points adjacent to the maximum point to form a parabola and then choose the maximum value of it as the final result. This method prevents the estimation result from limiting by the resolution. After this procedure, the cable length and position displacement can be estimated and used for the following data processing.

2.4. NUMERICAL SIMULATION

A simulation can first be implemented to check the feasibility of the method explained in the last section. The author chose a map of a part of Delft(figure 2.3), then transferred the image to the gray value data set; the type of color represents the average RCS of this area.

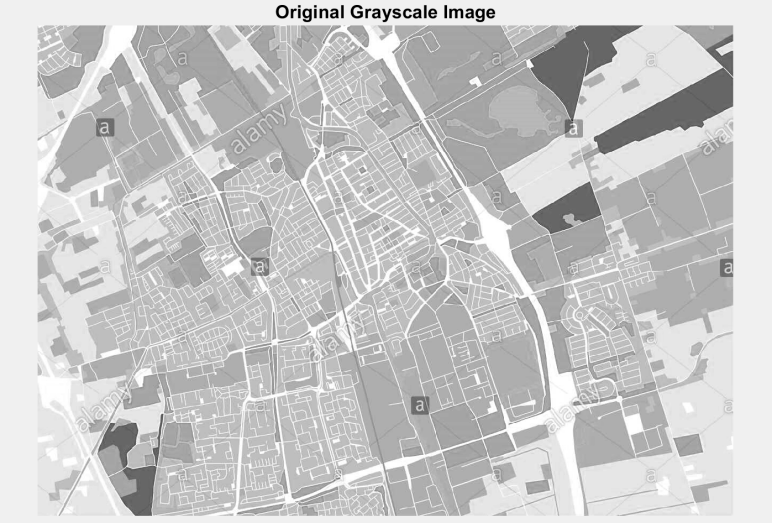

Figure 2.3: Map of Delft

2.4.1. CABLE LENGTH ALIGNMENT

The parameters of radar 1 and 2 have been set using the values in table 2.1, then the image data can be interpolated to the radar coordinates.

	Radar 1	Radar 2
Range grid step [m]	2	3
Angular grid step [deg]	0.5	0.5
Max range [m]	800	800
Cable length of radar [m]	0	45

Table 2.1: Parameters of the radars for spatial alignment simulation

Assuming the position displacement is [δx, δy] = [10m,20m], the PPI images for radar 1 and radar 2 were created (See figure 2.4(a) and 2.4(c)). An antenna beam with a Gaussian shape in elevation has been added to the original data to simulate a real data scan. Zero mean Gaussian noise has also been added to the data. The azimuth-range plots of the two radars are plotted in figure 2.4(b) and 2.4(d).

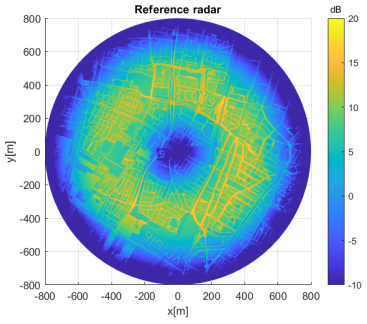

(a) PPI image of radar 1

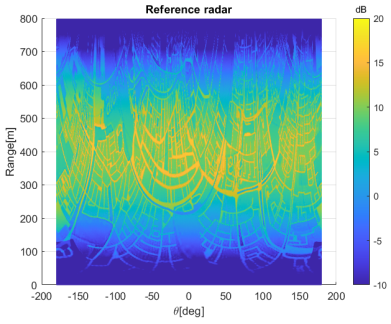

(b) Azimuth-range plot of radar 1

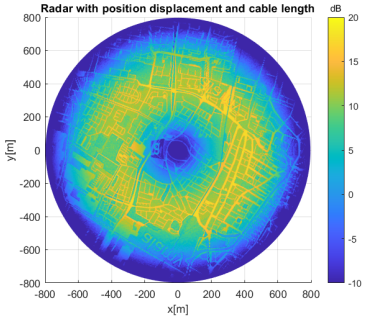

(c) PPI image of radar 2

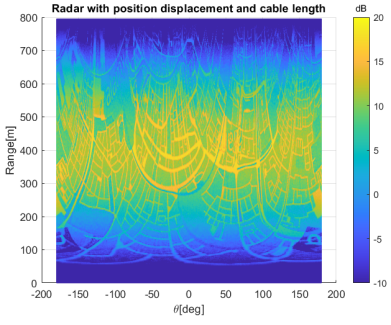

(d) Azimuth-range plot of radar 2

Figure 2.4: PPI image and azimuth-range plot of the two radars

Because the x, y displacement of two radars is much smaller than the range of the observed scene, and for the i-th target, $\theta_P^i \approx \theta_M^i$, where M and P denote the measurements of PARSAX and MESEWI, respectively, the azimuth displacement of the two radars can be ignored.

Using equation 2.2, the cable length of radar two can be estimated. To prevent the contingency of the results, the results listed below are the average of one hundred Monte-Carlo simulations.

Figure 2.5 shows the result of the cable length estimation. In the plot, the maximum correlation value in the range axis is 44m, close to the cable length set before. The second dimension (Angle) is added to verify that no angular misalignment occurs, which has been mentioned in the hypothesis (section 2.3).

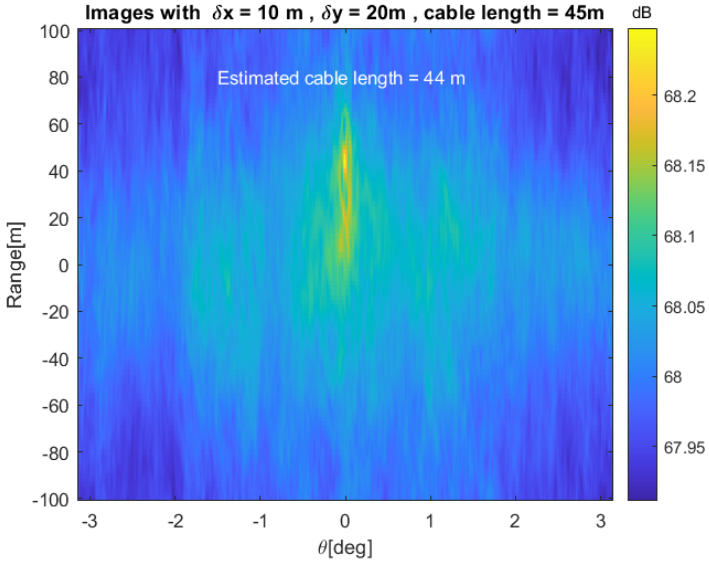

Figure 2.5: Correlation result in polar coordinate

After the procedure explained above, the cable length value of the second radar has been obtained; this value can be used to do the data compensation. The result before and after compensating the cable length in range axis infusing the azimuth-range image of the two radars are shown in figure 2.6. The images of the two radars were plotted in the same figure with different color bars. The color bar for the reference radar is in blue, and the one with cable length is in orange.

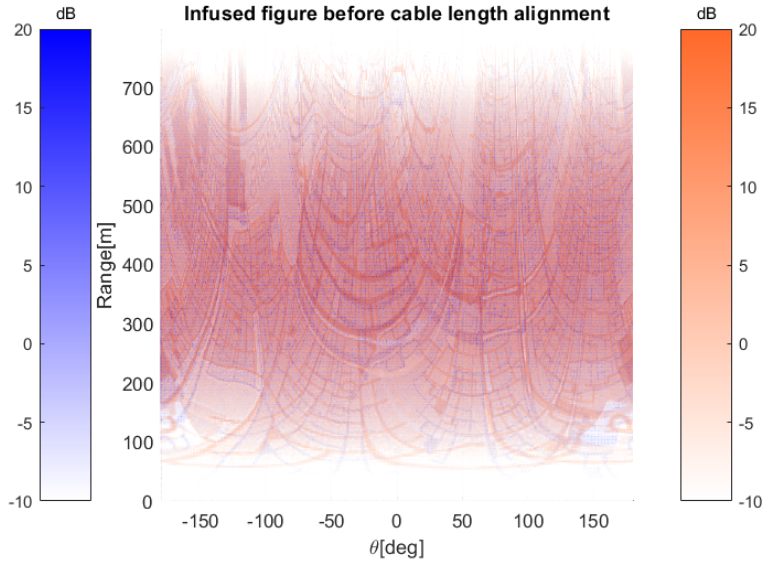

(a) Before cable length alignment

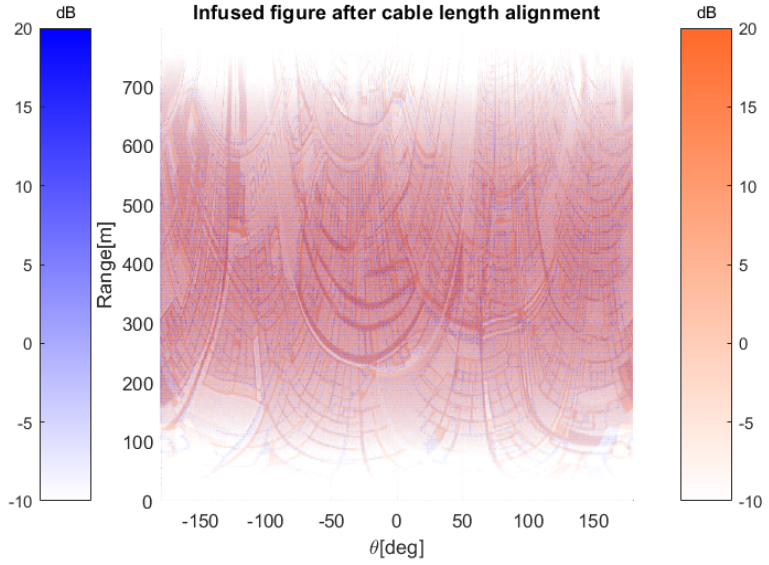

(b) After cable length alignment

Figure 2.6: The infused azimuth-range image of the two radars

In figure 2.6(b), we can see that, compared to 2.6(a), the cable length has been compensated in the range axis, and there is still a certain displacement, which corresponds to the position displacement of the two radars. At this step, we can switch to Cartesian

coordinate and do the cross-correlation again to estimate the position.

2.4.2. POSITION ALIGNMENT

Since the position displacement is in Cartesian coordinates, the data should be interpolated to Cartesian coordinate first using equation 2.3. The value for the x and y-axis for the Cartesian domain processing is set to make sure the rectangular Cartesian plot is within the PPI circle. Figure 2.7 shows the radar image in Cartesian coordinates.

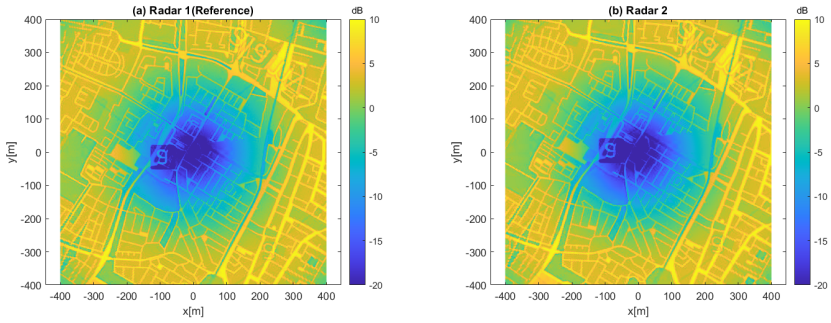

(a) Reference radar (b) Radar 2 with position displacement

Figure 2.7: Radar image in Cartesian coordinates

The displacement of the two plots can be estimated using equation 2.3. The correlation result is shown in figure 2.8.

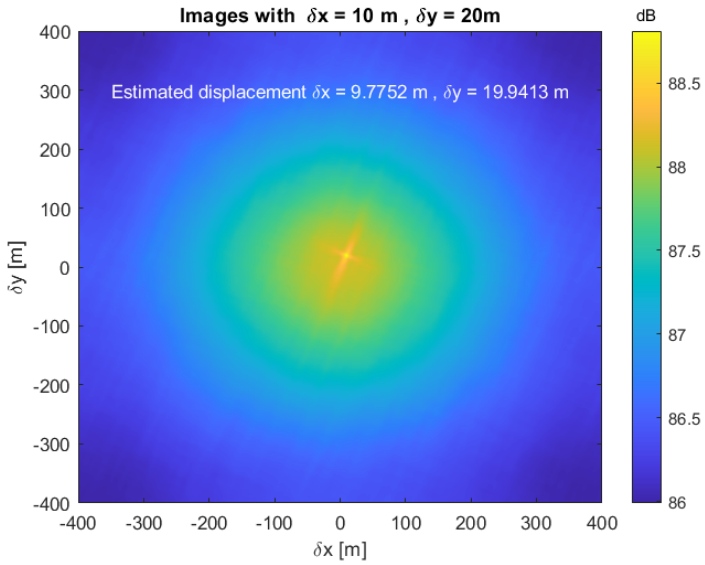

Figure 2.8: Correlation result in Cartesian coordinate

After using this value to do the data compensation, the infused PPI images of the two radars are shown in figure 2.9. In figure 2.9(c), it is clear that the two radars' images fully coincide with each other after cable length and position alignment, which means the spatial alignment procedure is successful.

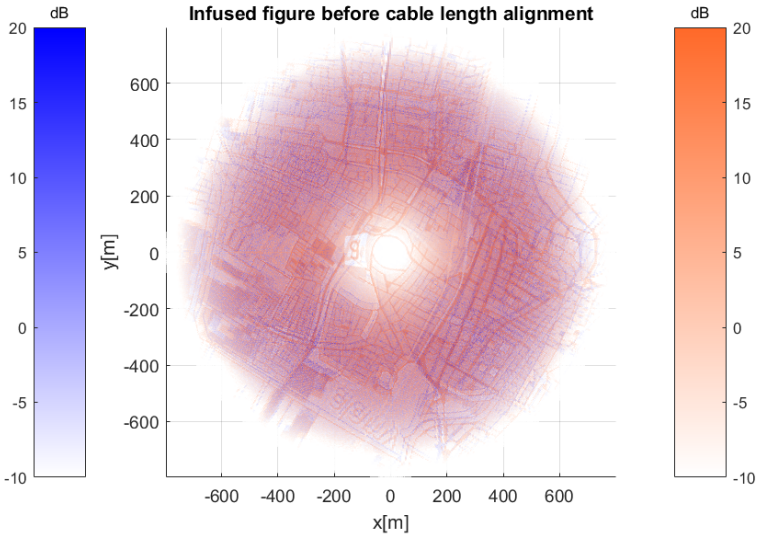

(a) Original infused figure

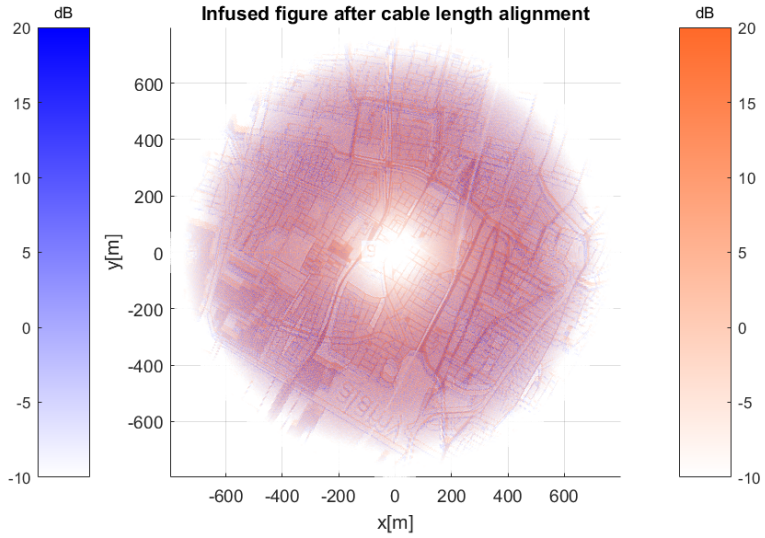

(b) After cable length alignment

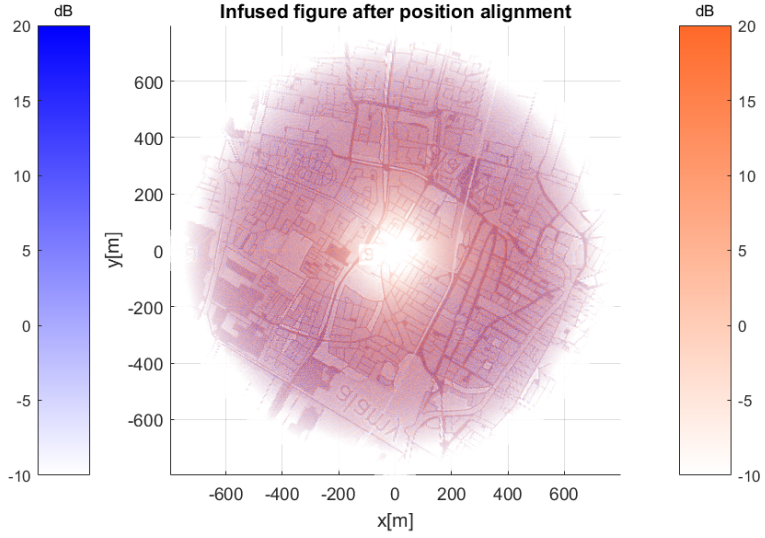

(c) After position alignment

Figure 2.9: The infused PPI image of the two radar in Cartesian coordinate

To investigate the similarity of radar images before and after processing, the structural similarity index (SSIM) [47] was calculated at every processing step. The SSIM value is between 0 and 1, the closer to 1, the more similar the two images are. The results were averaged over 100 trials assuming the scene, shown in fig 2.10. In the figure, it is clear

that the similarity of the two radar images is increasing. After cable length and position alignment, the SSIM value is 0.9879, close to 1.

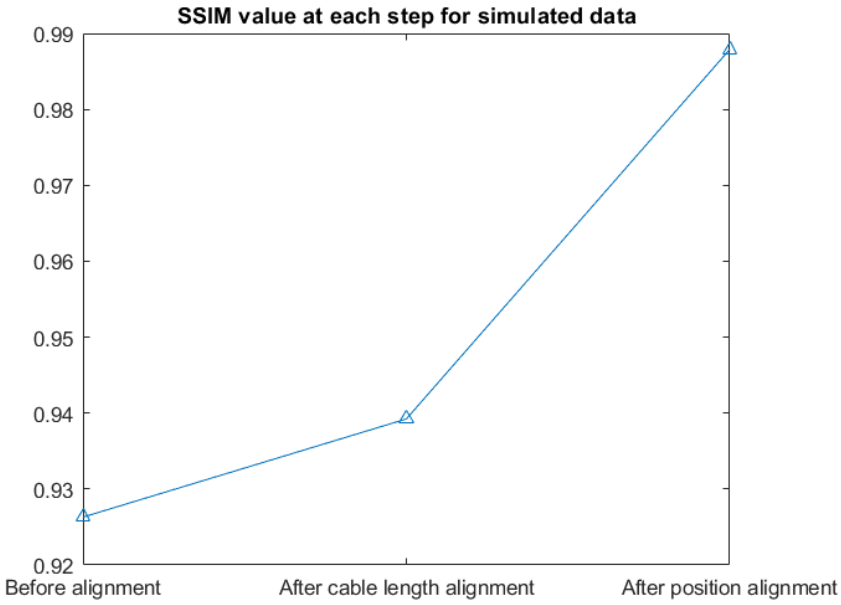

Figure 2.10: SSIM value at each processing step for simulated data

In order to investigate the effect of radar parameter settings and the choice of experimental pictures, several simulations have been implemented with one parameter changing, and the SSIM value curves are listed in figure 2.11.

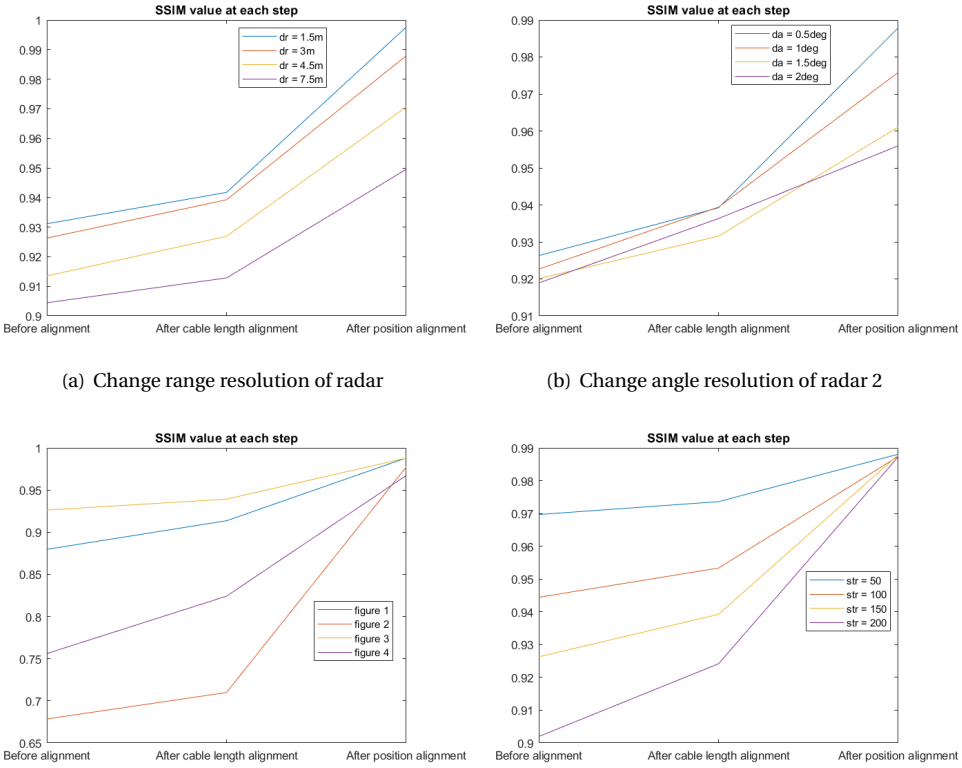

(a) Change range resolution of radar

(b) Change angle resolution of radar 2

(c) Change to other maps for processing

(d) Change the antenna beam-width

Figure 2.11: SSIM curve for different parameters

From figure 2.11(a) and 2.11(b), we can conclude that high range and angle resolution results in better alignment performance. The maps chosen for 2.11(c) are the maps for Den Haag from Google search; the difference of picture resolution and the contrast and degree of difference in different areas of the pictures could have some influence on the calculating of SSIM values. The str value in figure 2.11(d) is the standard deviation of the Gaussian shape. The antenna beamwidth would be wider with a larger str value.

2.5. EXPERIMENTAL VALIDATION

The actual data was collected on 2021-05-11, and the measurements were done at low power for H and V with 10 dB attenuation. The parameters of the two radars are in table 2.2.

	PARSAX	MESEWI
Central frequency [GHz]	3.3	9.6
Range resolution [m]	3	3
Elevation angle [deg]	-2	-1.872

Table 2.2: Parameters of PARSAX and MESEWI

The original azimuth-range plots, PPI images of the two radars are shown in figure 2.12 and 2.13, respectively.

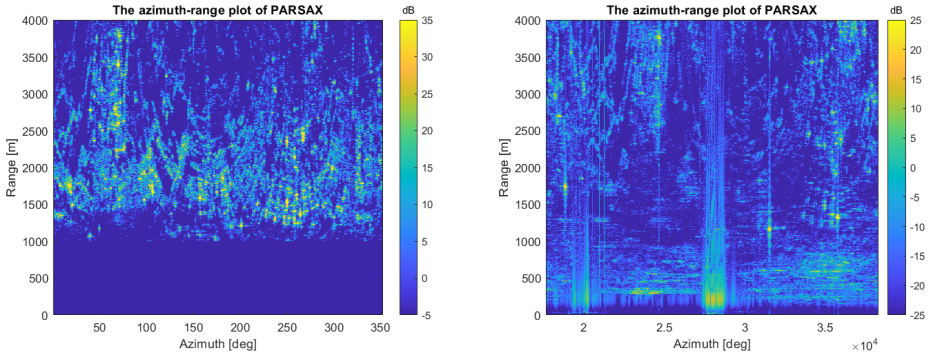

(a) PARSAX (b) MESEWI

Figure 2.12: Original azimuth-range plot of PARSAX and MESEWI

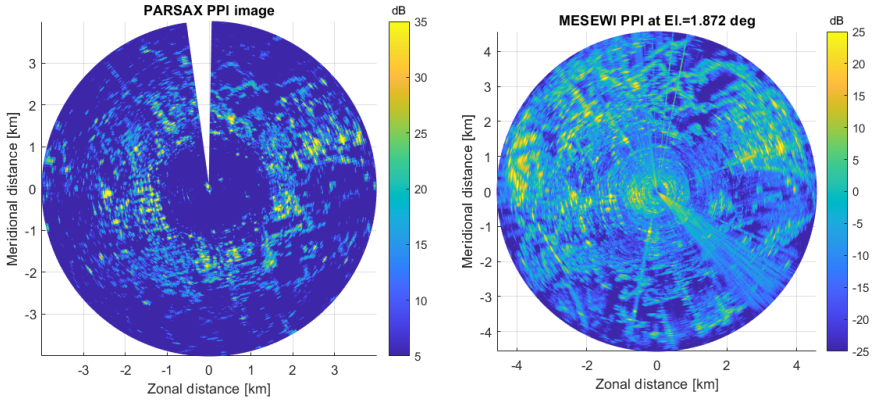

(a) PARSAX (b) MESEWI

Figure 2.13: Original PPI image of PARSAX and MESEWI

In figure 2.12(b), we can see that there are several messy reflections in close range, which can be the reflections from the rooftop near the two radars. By replacing the re-

flections from 0 to 1000m with zero, interference from roof reflections can be avoided. What is more, due to the measurement setup, the azimuth axis for MESEWI does not start from 0 degrees like the one for PARSAX, so we need to rearrange the data of MESEWI. The results are shown in figure 2.14.

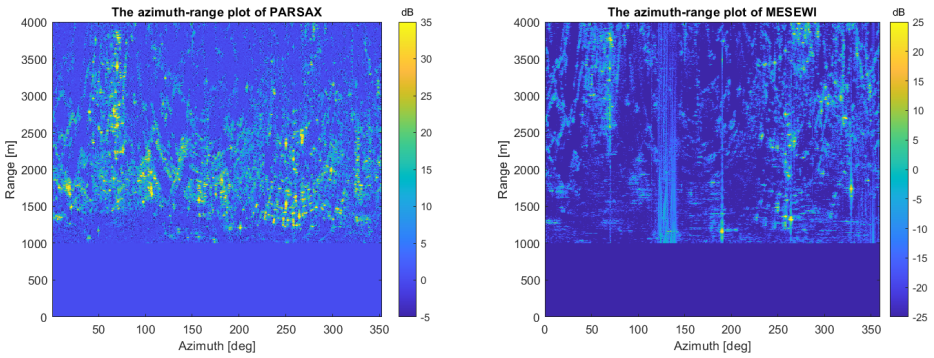

(a) PARSAX (b) MESEWI

Figure 2.14: Azimuth-range result of PARSAX and MESEWI(after rearranging and cutting the reflections from rooftop)

2.5.1. CABLE LENGTH ESTIMATION

Since the angle grid step of the two radars is different, the data should first be interpolated in the exact grid and then do the cross-correlation. Using equation 2.2, the cable length of PARSAX is around 36.67m(see figure 2.15). Using the method in [15], find the maximum value of the parabola formed by the maximum and the two adjacent points. This result is optimized to 36.83m; this value is used for the data compensation.

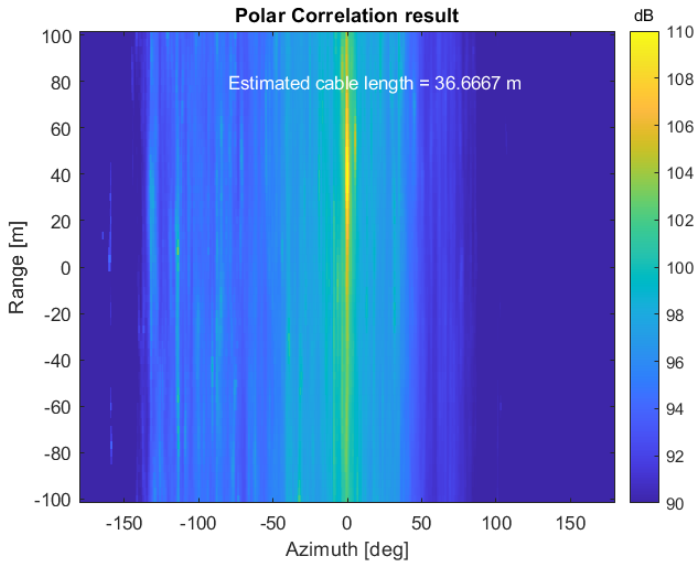

Figure 2.15: Correlation result in polar coordinate

The result after compensating the cable length in the range axis for PARSAX and infusing the PPI image of the two radars in polar coordinates is shown in figure 2.16; the result in Cartesian coordinates is shown in 2.17. The one with the blue color bar is MESEWI, and the orange one is PARSAX. In figure 2.16, at around 260deg and 1250m, there is a small part where the effect of cable length alignment can be seen. The coincided part after cable length alignment increased.

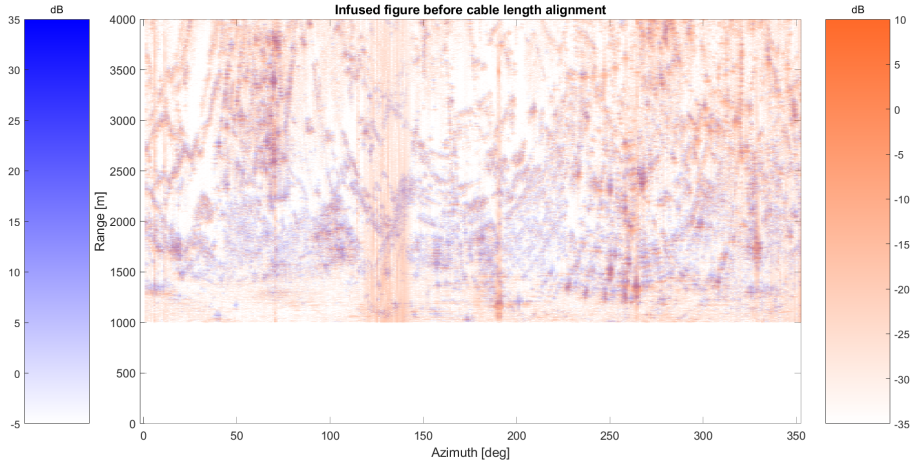

(a) Before cable length alignment

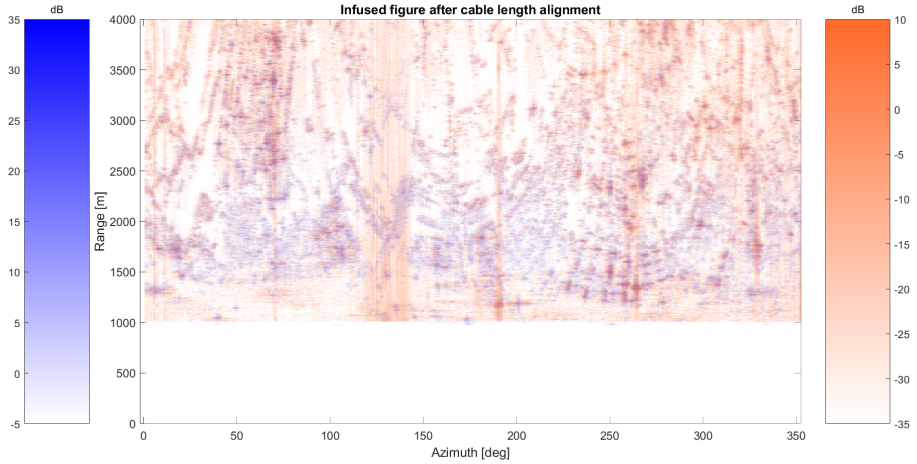

(b) After cable length alignment

Figure 2.16: The infused PPI image of the two radar in polar coordinate

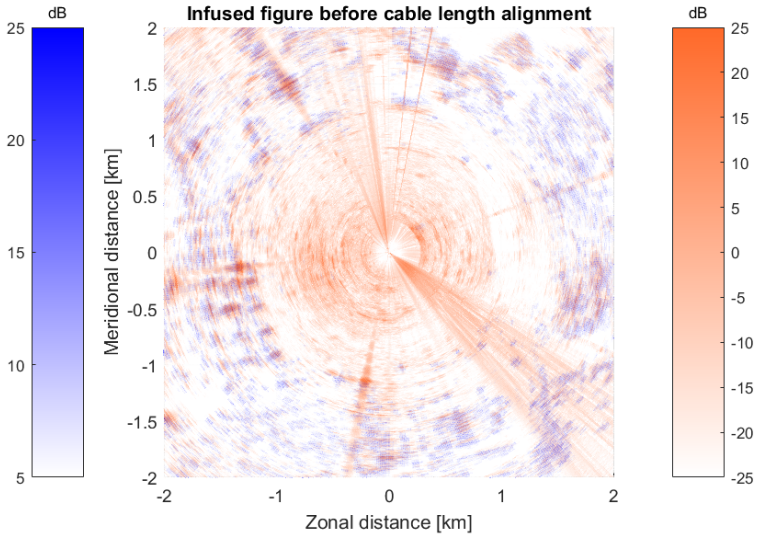

(a) Before cable length alignment

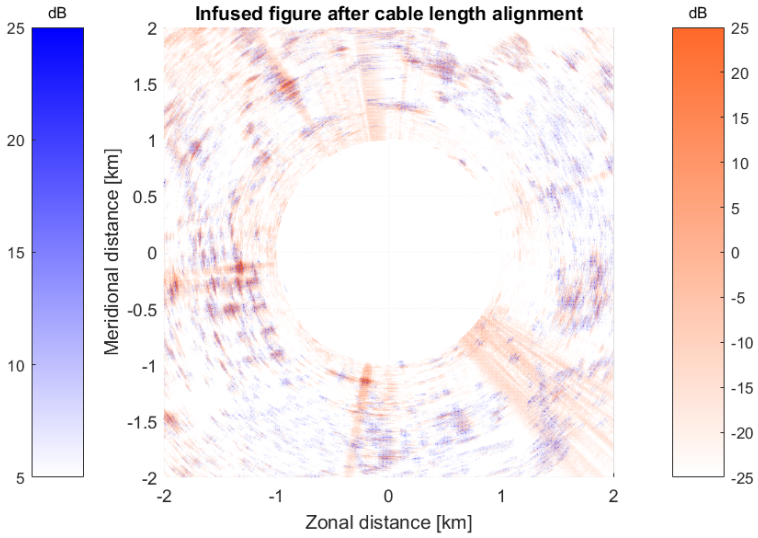

(b) After cable length alignment

Figure 2.17: The infused PPI image of the two radar in Cartesian coordinate

2.5.2. POSITION DISPLACEMENT ESTIMATION

We have already done the cross-correlation in polar coordinates to estimate the cable length of PARSAX.However, the position displacement of the two radars is in Cartesian coordinates, so the data should be interpolated to Cartesian coordinate first(See figure

2.18).

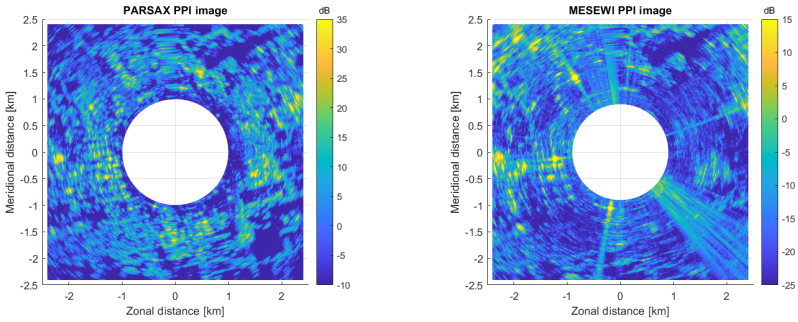

(a) PARSAX (b) MESEWI

Figure 2.18: Radar image in Cartesian coordinate

Using equation 2.3 to do the cross-correlation, the position displacement is around [δ x, δy] = [2.346m, -7.0381m](See figure 2.19). After parabola fitting, which uses the maximum point and two adjacent points to formulate a parabola and find the maximum point of the parabola in both x and y axis [15], the result is [2.3362m,-9.1327m]. This result is used for the final position alignment.

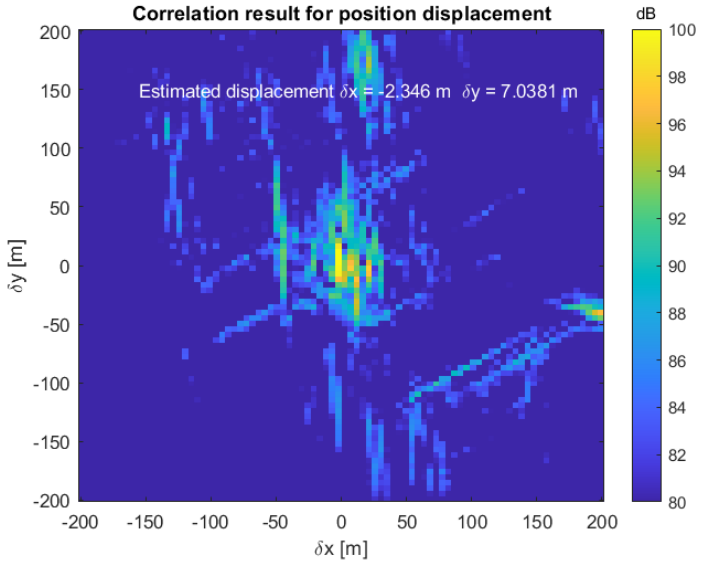

Figure 2.19: Correlation result of Cartesian data

The infused image before and after position alignment are shown in figure 2.20.

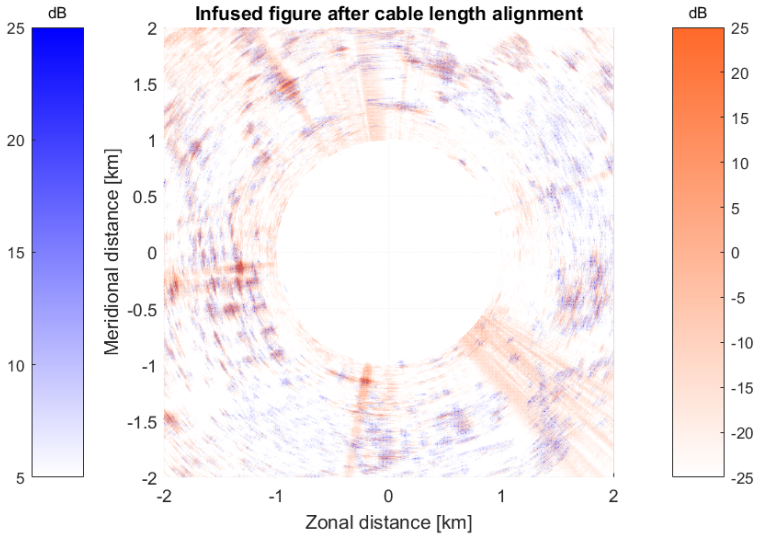

(a) Before position alignment

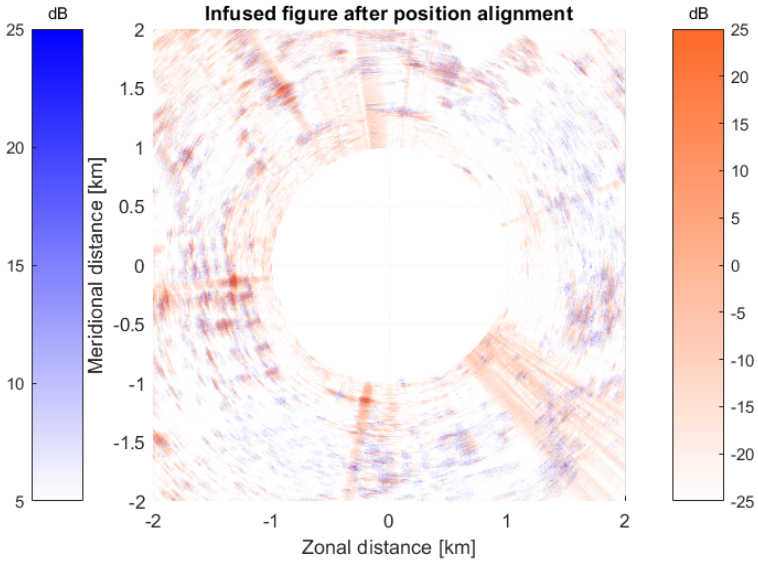

(b) After position alignment

Figure 2.20: The infused PPI image of the two radar in Cartesian coordinate

To check the accuracy of cable length alignment, we chose a pretty strong target. It is the chimney at around 190deg and 1100m from the rooftop of EWI. A picture of this chimney is in figure 2.21.

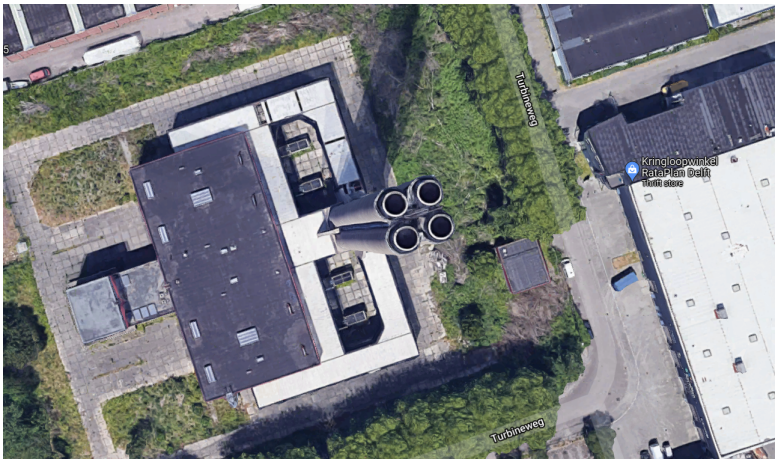

Figure 2.21: Photo of the chimney

The chimney in figure 2.22 was zoomed to its position. In figure 2.22(b) it is clear that after cable length compensation, the distances from the circle center to the chimney of the two radars become almost the same compared to figure 2.22(a), which means the cable length has been successfully compensated. As for position alignment, in figure 2.22(b), there is a small offset of the chimney in the two plots, and in 2.22(c), the target is almost coincided with each other, which shows a relatively ideal data calibration result.

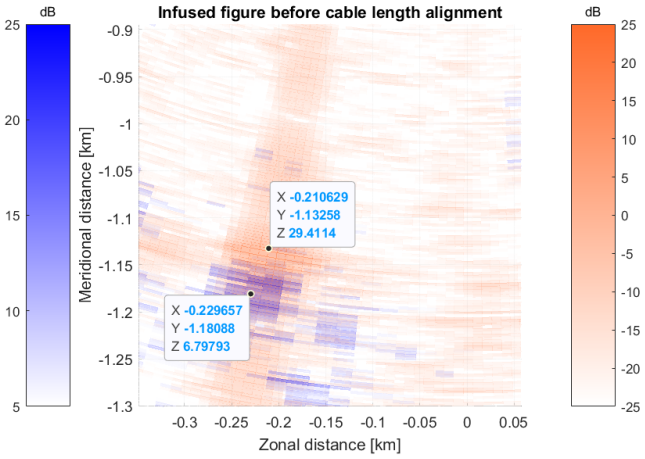

(a) Original infused figure

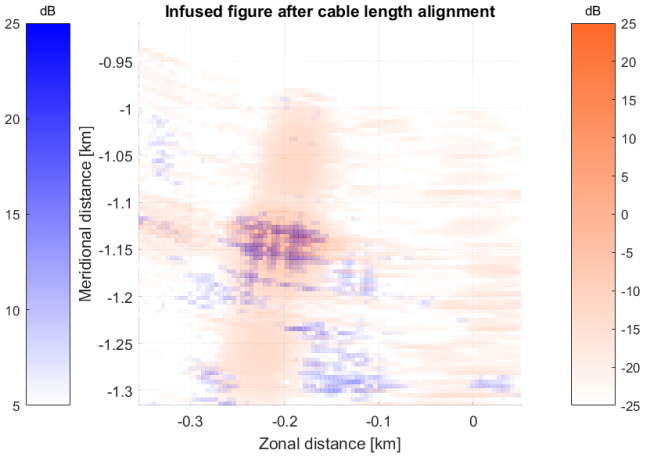

(b) After cable length alignment

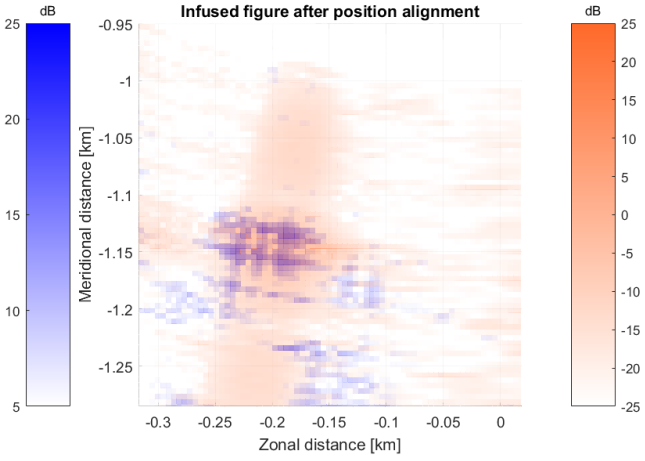

(c) After position alignment

Figure 2.22: The infused PPI image of the two radar in Cartesian coordinate

The SSIM value for actual data after each step has also been calculated; the result is in figure 2.23. The value after spatial alignment does not approach one as the simulations because of RCS variation vs. frequency. However, it increases after each alignment step, which means that the data becomes more similar after the proposed processing; this is what we expected from the result of actual data.

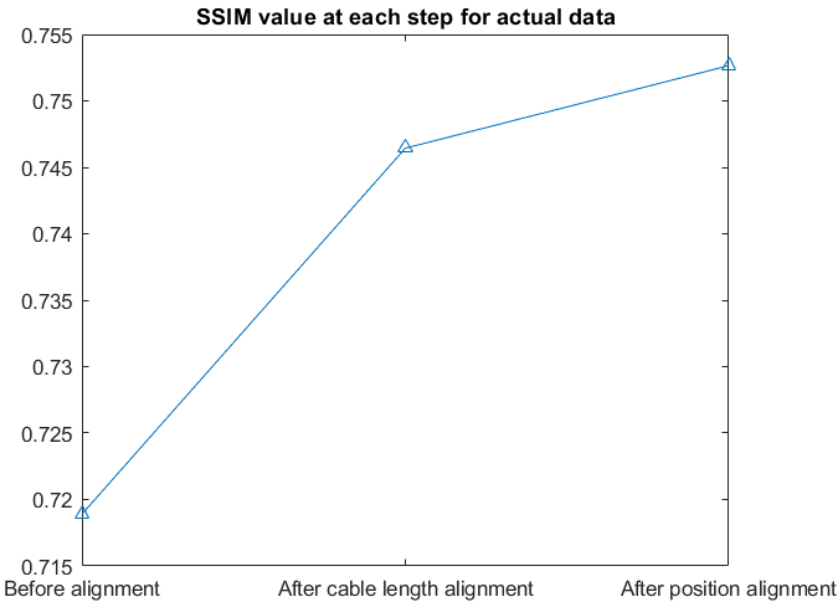

Figure 2.23: SSIM value at each processing step for actual data

2.6. CONCLUSION

In this chapter, a feasible method for spatial alignment of two independent radars' data has been explained and tested with numerical simulation and actual data. The infused result of the simulation shows that the feasibility of this method and its accuracy are relatively satisfactory. The SSIM value after data alignment in the simulation part is 0.9879, which is close to 1; this means the similarity of the two images after spatial alignment is very high. The result for actual data has an acceptable offset compared to the accurate position displacement because of the measurement setup. Moreover, the SSIM value after each step increases, so the figures are more similar after data alignment. In general, the alignment in the spatial domain has significantly reduced the deviation of the data, which would be a great help for the following processing.

3

TEMPORAL ALIGNMENT

In this section, the problem of the temporal alignment of two radars is addressed. The cross-correlation method is applied to the measurements of moving targets observed by both radars to estimate the time shift between the sensors. The proposed method is validated with simulation and applied to an actual data set.

3.1. INTRODUCTION

In order to perform an accurate pre-processing analysis, it is crucial to align the experimental data in the time domain. It is also essential to identify the delays between different measurement systems to correctly align each data set so that the data from each system can be combined for analysis; this is particularly important for information fusion applications [41]. Some temporal alignment methods have been proposed up to now, e.g., Dynamic Time Warping (DTW) [40],Hidden Markov Models(HMM), Recurrent Neural Networks(RNN) or Action Spectogram [45, 25, 29]. In this project, because the two radars work independently with different processing procedures and are not synchronized, there will be a difference in the time for the two radars to receive the signal returned by the same moving target (the time stamps in both radars are with a second accuracy). We need to estimate and compensate for this time shift error to increase the following data processing accuracy. As the procedure in spatial alignment, the simulation part was used to check the method feasibility; then, the applicability of the proposed method is demonstrated on an actual data set.

3.2. PROBLEM STATEMENT

The problem in time alignment is to synchronize the two radars' data to the same starting time. In the presence of moving targets, the time can be estimated from the data. In this project, the two radars have a slight time difference guaranteed by GPS/PC time. This alignment ensures that the inputs of data fusion are the measurements of the same target simultaneously.

3.3. PROPOSED TEMPORAL ALIGNMENT METHOD

3.3.1. DATA MODEL

A pulse-Doppler radar with wideband waveform is considered. In this chapter, we assume the wideband radar illuminates a moving point-like target. The wideband radar transmits a coherent burst of M wideband pulses in the CPI. A range migration of a moving scatterer at blind velocity is assumed to be negligible within one Pulse Repetition Interval(PRI). In this model, low Pulse Repetition Frequency(PRF) mode is considered, assuming no range ambiguities occur. Using the result in [37], the signature for a point-like moving target in the fast-frequency domain can be expressed as

$$\mathbf{T}_{ff,st}(l,m) = \frac{1}{K} e^{j2\pi f_D T_r m} e^{-j2\pi \frac{k_0}{K} l} e^{j2\pi \frac{v_0 T_r}{\delta R K} lm} \tag{3.1}$$

Where K is the number of range- cells, f_D is the Doppler frequency, T_r is the sweep time, m is the slow time axis, k_0 is the corresponding range cell of the target, l is the range axis, v_0 is the velocity of the target, δR is range resolution.

Using this signature, the echo of a point-like target $\mathbf{A}_{wb}$ can be expressed as

$$\mathbf{A}_{wb} = a\mathbf{T}_{ff,st}(l,m) + \mathbf{n} \tag{3.2}$$

where a is a complex amplitude, $\mathbf{n}$ is the zero mean Gaussian noise.

3.3.2. PROPOSED SOLUTION

The slow time schematic diagram of the two radars can be seen in figure 3.1. We only consider one target with constant velocity moving away from the radar. The slope of the line is the velocity of the target. Because we assume the target is moving away from the radar, the distance increases with time.

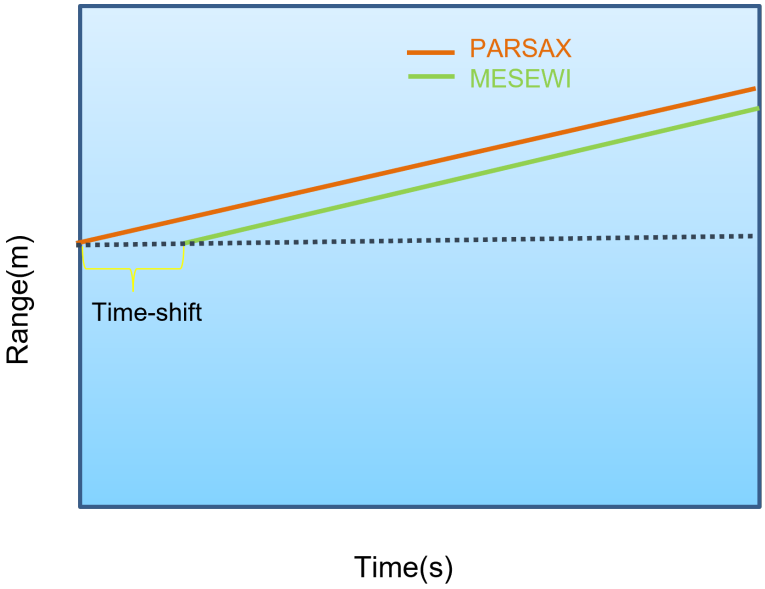

Figure 3.1: Schematic diagram of the two radars

In figure 3.1, because the two radars work independently with no synchronization information, there would be an offset between the two trajectories of the target in the slow time image. Therefore, we can use the cross-correlation method to estimate this offset. Using equation 3.3, the time and range shift of the two radars can be obtained.

$$[\hat{\delta}t, \hat{\delta}r] = \underset{t}{\operatorname{argmax}} \sum_{i=1}^{k} \sum_{j=1}^{k} (\mathbf{S}_p(t_i^P, r_j^P) \otimes \mathbf{S}_m(t_{k-i}^M, r_{k-j}^M)) \tag{3.3}$$

Where $\hat{\delta}t$ represents the time shift and $\hat{\delta}r$ represents the range shift, matrix $\mathbf{S}_p$ and $\mathbf{S}_m$ represent the image of PARSAX and MESEWI in slow time domain, t_i^P is the i-th time cell of PARSAX and r_j^P is the j-th range cell of PARSAX, the t_i^M and r_j^M are the time and range for MESEWI. Since we already have the range shift value from the last chapter, the data can first be compensated in the spatial domain, and this cross-correlation method can be used to verify the accuracy of the results.

3.4. NUMERICAL SIMULATION

3.4.1. TIME SHIFT ESTIMATION PROCEDURE

Fast-moving targets may not be contained into a single range gate but migrate in range during the coherent processing interval (CPI), which is called the range migration phenomenon[5, 38]. Therefore, range gate walk must be taken into account to preserve the coherent integration gain. The fast coherent integration and the Hamming window along range and velocity domain have been applied in this simulation. The effect of coherent integration can be seen in figure 3.2. The target appears more focused after fast

CI.

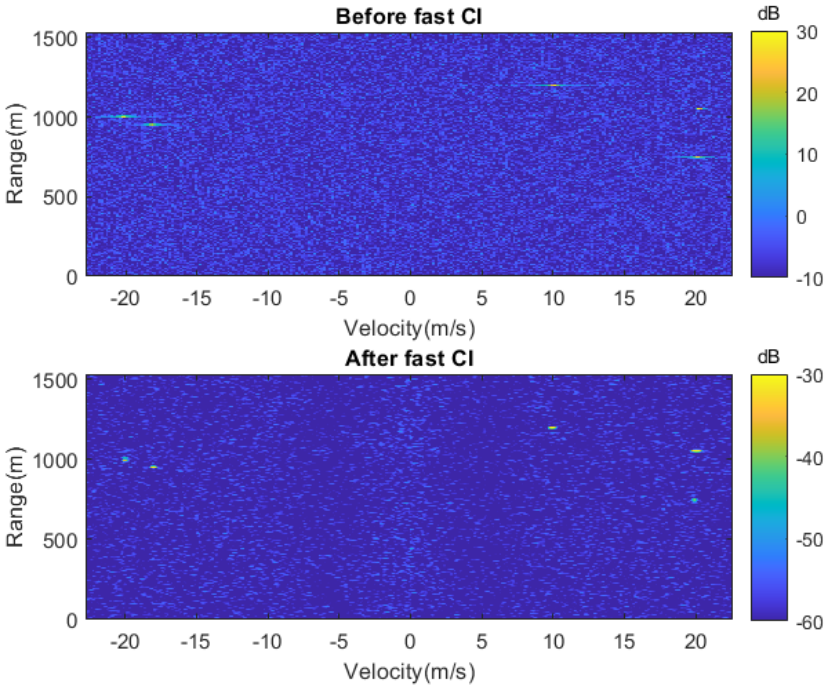

Figure 3.2: Performance of fast coherent integration

Using the reflected signal model from the target in equation 3.1 and 3.2, five moving targets have been created, the range and velocity of these targets are listed in table 3.1.

Target	Range(m)	Velocity(m/s)
1	1000	-20
2	1200	10
3	1050	-25
4	950	-18
5	750	20

Table 3.1: Moving target information

With SNR = 30, δR = 3m, T_r^P = 1ms, T_r^M = 0.61ms, the slow-time plot and Doppler-range plot of the two radars have been created in figure 3.3, each line represents a target, the slope of the line in time-range plot represents the target velocity. The Hamming window has been applied to the data in the range domain to suppress the sidelobes.

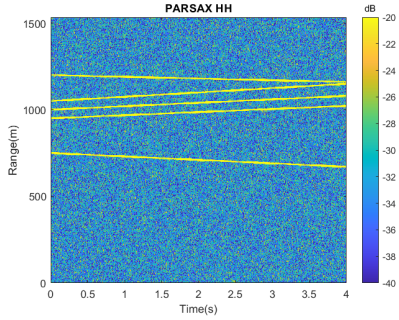

(a) Slow-time image for PARSAX

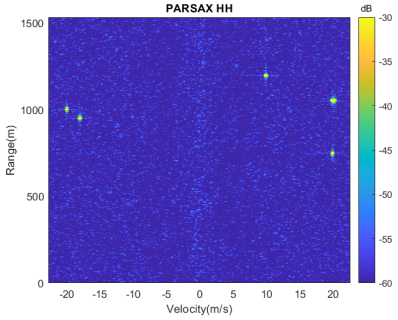

(b) Range-Doppler plot of PARSAX

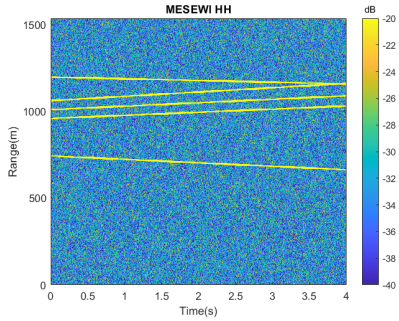

(c) Slow-time image of MESEWI

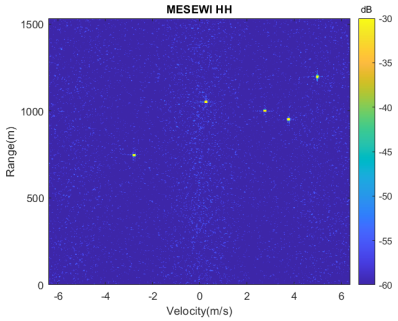

(d) Range-Doppler plot of MESEWI

Figure 3.3: The slow-time image and Range-Doppler plot of the two radars

In order to find the time shift between the two radars, the cross-correlation of the time-range plot can be used. Using equation 3.3, we can obtain the time and range shift of the two time-range plots.

Since in chapter 2, the range shift has been estimated, this valve could be used to do the range compensation for the two radars' data—-$\hat{\delta r}$ will be 0. Then what we get from equation 3.3 would be the time shift of the two radars. The correlation result is in figure 3.4.

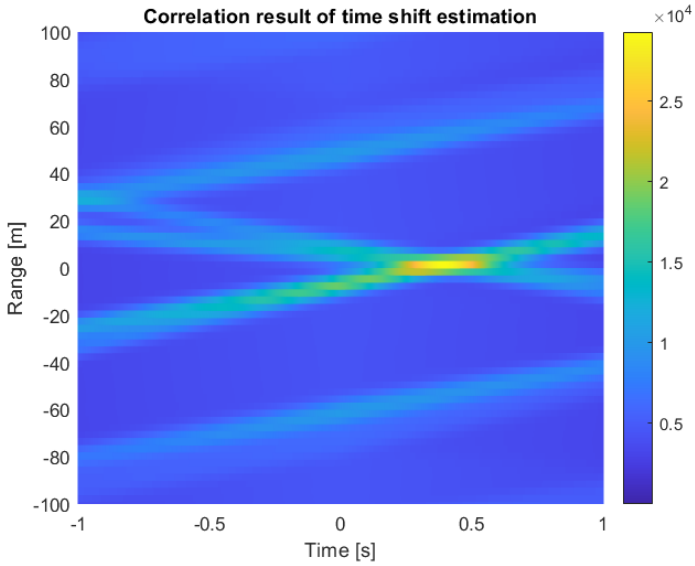

Figure 3.4: Correlation result of time shift estimation

3.4.2. PERFORMANCE ASSESSMENT

This section analyzes the influence of SNR, range resolution, PRI, and the processing time on the time shift estimation result. The number of samples used for Monte Carlo is 100. The time shift set for the two radars in this simulation is 0.4s. We assume that the range shift has already been compensated, so only the time shift estimation is considered in this section. In order to ensure the rationality of the results, we keep other parameters unchanged when changing one parameter. Means squared error(MSE) [39] is chosen to evaluate the estimation accuracy. If n times Monte Carlo estimations are generated, with $\hat{T}_i$ being the i-th estimation of the time shift and T_{shift} being the true time shift, then the within-sample MSE of the time shift error is computed as

$$MSE = \frac{1}{n}\sum_{i=1}^{n}(\hat{T}_i - T_{shift})^2 \tag{3.4}$$

i) The relationship between time shift estimation error and SNR

$t_{processing} = 4s$, $Tr_p = 1ms$, $Tr_m = 0.61ms$, $dR = 3m$, $T_{shift} = -0.4s$		
	mean(s)	var
SNR = 10	0	1.5718e-9
SNR = 15	-0.3726	4.9979e-6
SNR = 20	-0.3866	1.9142e-8
SNR = 30	-0.3919	4.8967e-9
SNR = 40	-0.3923	5.2131e-10
SNR = 50	-0.3923	0

Table 3.2: The mean time shift and variance with the changing of SNR

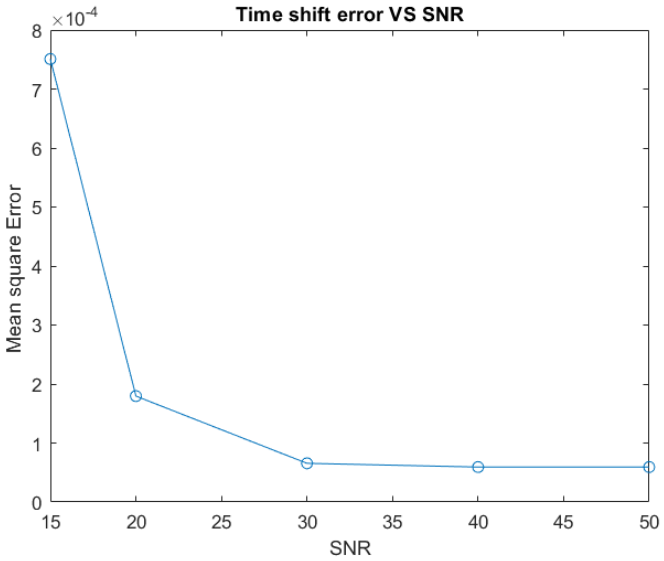

Figure 3.5: Time shift error vs. SNR

Looking into table 3.2 and figure 3.5, the relationship between time shift error and SNR is quite clear. Below 10dB, when the target could not be seen clearly, the estimation of the time shift can not be implemented because we use the shift of the target's trajectory to determine the shift in the cross-correlation method. When SNR is over 15dB, as SNR increases, the signal becomes more vital than noise; the absolute time shift error decreases, the same with the estimation variance; this is reasonable because, with lower noise influence, the time shift estimation should be more accurate.

ii) The relationship between time shift estimation error and range resolution

$t_{processing} = 4s$, $Tr_p = 1ms$, $Tr_m = 0.61ms$, $SNR = 30dB$, $T_{shift} = -0.4s$		
	mean time shift (s)	var
dR = 3	-0.3924	4.5751e-07
dR = 6	-0.3707	1.3636e-06
dR = 9	-0.3364	2.6109e-06
dR = 12	-0.2921	6.8211e-06
dR = 15	-0.2425	1.9449e-05

Table 3.3: The mean time shift and variance with the changing of range resolution

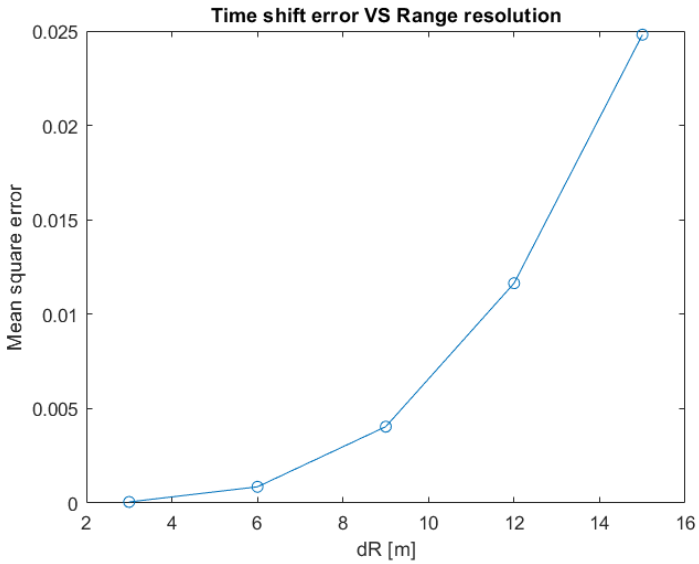

Figure 3.6: Time shift error vs. range resolution

Looking into table 3.3 and figure 3.6, we can see that a higher range resolution corresponds to a minor absolute error of time-shift estimation.; this is also reasonable because higher resolution means more precise measurement, which is favorable for cross-correlation.

iii) The relationship between time shift estimation error and sweep time

In this section, since the PRI of the two radars are different, different PRI values of MESEWI have been chosen to run the simulation, and the PRI for PARSAX is 1ms. Before cross-correlation processing, the two radar data should be interpolated to the same size to ensure each pixel's size for correlation is the same. The result is shown in the table and the figure below.

$t_{processing} = 4s$, $Tr_p = 1ms$,$dR = 3m$, $SNR = 30dB$, $T_{shift} = 0.4s$		
Tr_m	mean(s)	var
0.6e-3	-0.3926	3.2820e-07
0.8e-3	-0.3918	2.7009e-07
1e-3	-0.3904	2.9846e-07
1.2e-3	-0.3920	4.6728e-07
1.4e-3	-0.3925	2.8494e-07
1.6e-3	-0.3916	6.1311e-07
1.8e-3	-0.3912	9.8424e-07
2e-3	-0.3926	1.4983e-06

Table 3.4: The mean time shift and variance with the changing of PRI of MESEWI

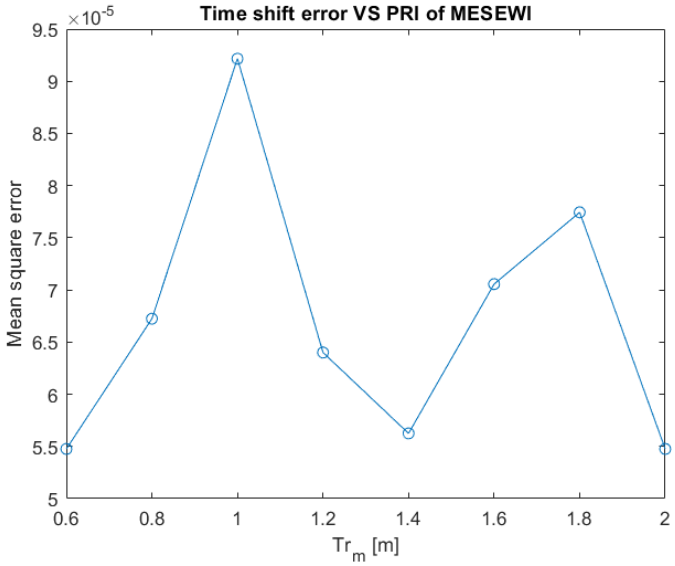

Figure 3.7: Time shift error vs. PRI of MESEWI

In this section, the changing of PRI does not have much influence on the MSE. The change of MSE is irregular. So we can assume that the change of PRI would not have much influence on the time shift estimation.

iv) The relationship between time shift estimation error and processing duration

$dR = 3m$, $Tr_p = 1ms$, $Tr_m = 0.61ms$, $SNR = 30dB$, $T_{shift} = -0.4s$		
Duration(s)	mean time shift(s)	var
2	-0.3858	1.1775e-07
3	-0.3921	9.8198e-06
4	-0.3944	1.2389e-06
5	-0.3950	1.6809e-08
6	-0.3962	6.0494e-07
7	-0.3966	7.9081e-08
8	-0.3970	4.3250e-08

Table 3.5: The mean time shift and variance with the changing of processing duration

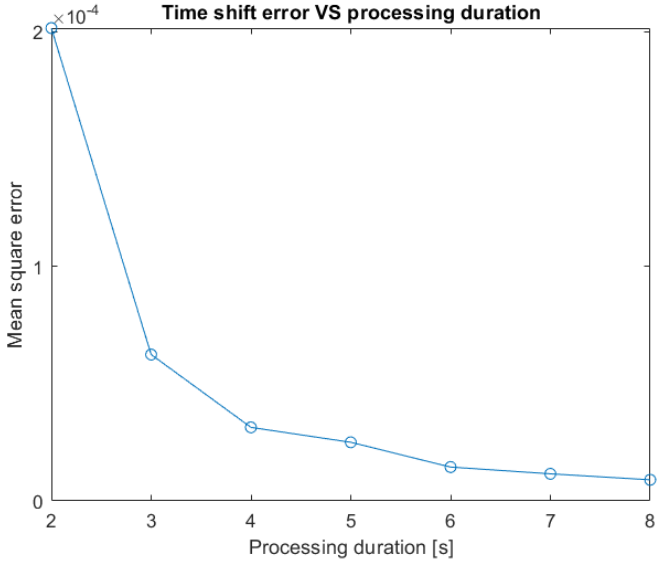

Figure 3.8: Time shift error vs. processing duration

In this section, the increasing duration time decreases the mean square error, the same as the variance. We can conclude that in this situation, if we assume that the targets are present in the antenna beam during the whole observation, the longer processing time provides better information for time-shift estimation.

3.5. EXPERIMENTAL VALIDATION

The method for time alignment has some similarities with the method for position alignment. The measurement of this alignment was done simultaneously for about a 1-minute scanning on highway N470. In figure 3.9, the orange rectangular part is the area of this measurement's scan, where the road is straight, and there is only one row of lanes in each direction.

Figure 3.9: N470 on Google map

The mode of PARSAX was fixed at a -2 degree elevation angle and 76-degree azimuth angle. MESEWI was at Azimuth 76 degree and elevation -1.5 degree. MESEWI is equipped with GPS modules that provide timestamps with 1 Hz. Furthermore, PARSAX relies on its system(PC) timer, synchronized timely via the Internet. The cross-correlation of the time-range plot can be used to find the time shift between the two radars. Because the systems are not synchronized, the processing times of PARSAX and MESEWI are different, which contributes to the different start times in the slow-time plot(see figure 3.10). After transferring the date-time value saved in the header file of the radar to UTC, the overlap period of the two radar data can be found.

From the measurement data file, we can get the information that PARSAX starts from 2021-06-29 08:16:03' and ends at 2021-06-29 08:18:38'. MESEWI starts from 2021-06-29 08:16:17' and ends at 2021-06-29 08:17:32'.The start and end frame of PARSAX for the correlation can be calculated using the duration of each frame of the two radars, which are 28 and 171, respectively.

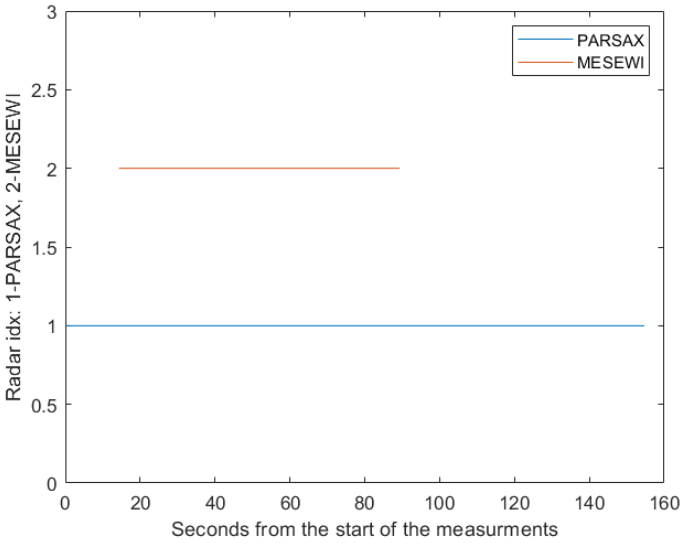

Figure 3.10: Measurement time of the two radars

The position offset of the two radars has been aligned using the cable length value from chapter 2. Figure 3.11 shows the slow time plot of the two radars after applying a three-pulse clutter canceller. The diagonal lines on the picture represent the moving targets on the highway.

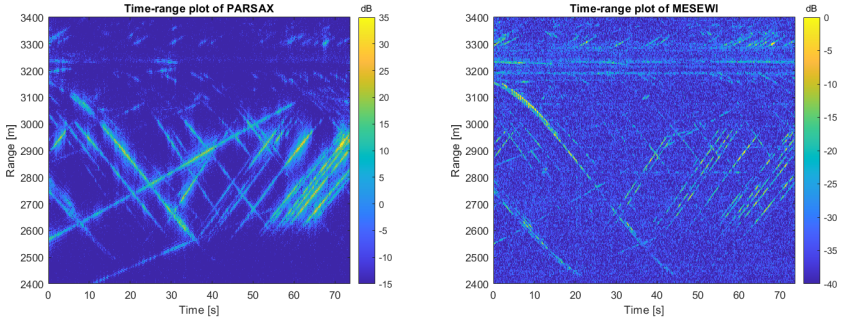

(a) PARSAX (b) MESEWI

Figure 3.11: Slow-time PPI image of the two radars' measurements

Before going to the cross-correlation procedure, the two radars' data should be interpolated to the same time resolution because of their different frame durations. In this project, the MESEWI data has been interpolated to PARSAX's time axis. Then, using equation 3.3, the cross-correlation can be implemented.

The correlation in range dimension was also implemented to check the correction of range alignment. A specific period (16 seconds) of the data was chosen to find a stable result of the time shift output. Cross-correlation with processing time 9.7s was done within this period and stepped 0.0734 each time. The result of estimation vs. start time of the processing are shown in figure 3.12.

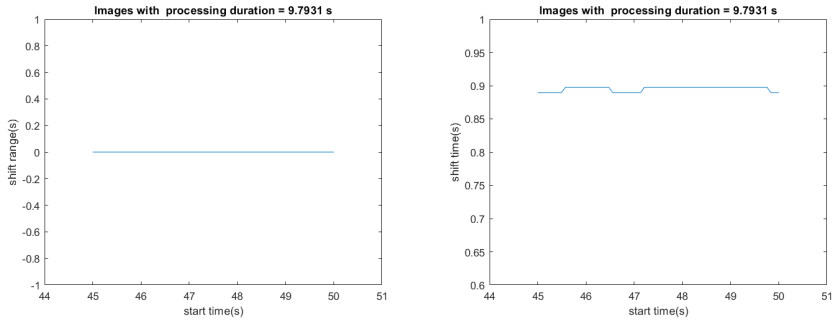

(a) Range shift

(b) Time shift

Figure 3.12: Time and range shift result

From the result in figure 3.12, the time offset is around 0.89s, and the range shift remains 0m, which means the spatial alignment is correct, and the value of the time offset can be used to do the time alignment. The result of the time alignment in slow time image can be seen in figure 3.13, in which the blue one represents the PARSAX's data, and the orange one is MESEWI's data. In figure 3.13(a), we can see that at around 3300m, there are several horizontal lines which are coincided, this means the data in range has already been compensated, and there exists a slight shift of the diagonal lines; this is because of the time shift. After time alignment, in figure 3.13(a) all the lines are coincident, which shows that the result of time alignment is reasonable.

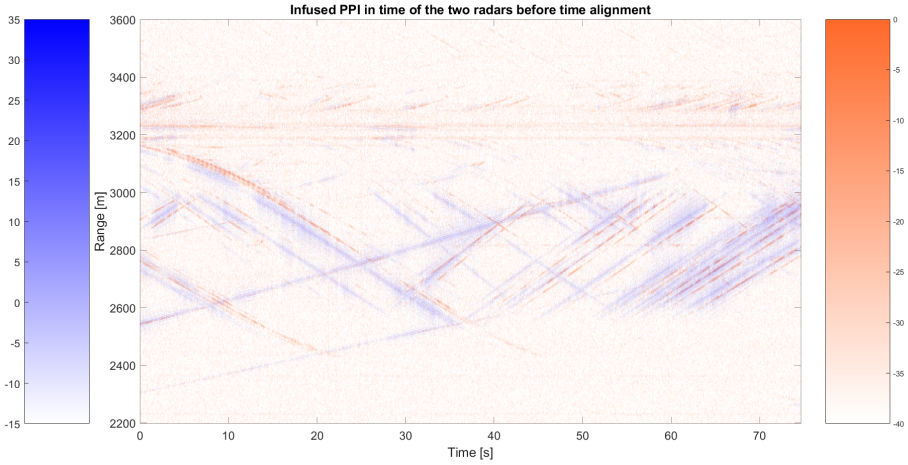

(a) Infused PPI in time before time alignment

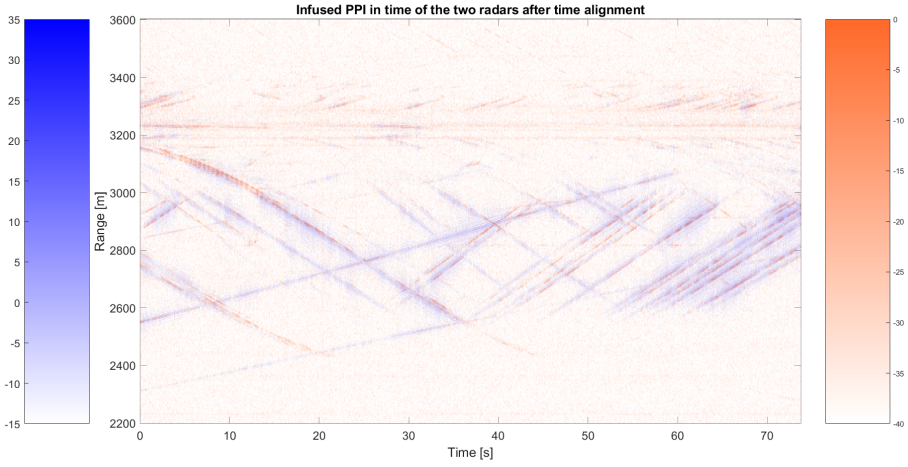

(b) Infused PPI in time after time alignment

Figure 3.13: Infused PPI in time figures of the two radars

We also checked the result of this time alignment procedure using the range-Doppler images of the two radars in figure 3.14. Figure 3.14(a) is the Doppler plot before data alignment and figure 3.14(b) is the Doppler plot after data alignment. The same target appears in the same position after data alignment.

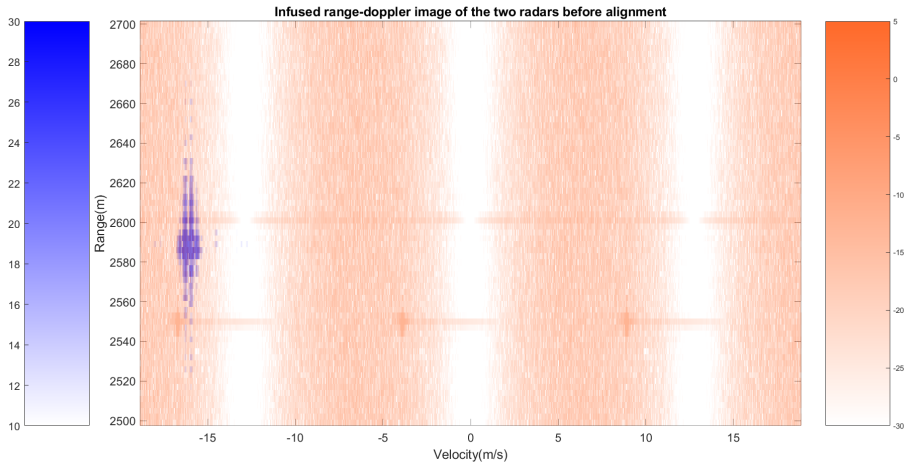

(a) Range-doppler figure before alignment

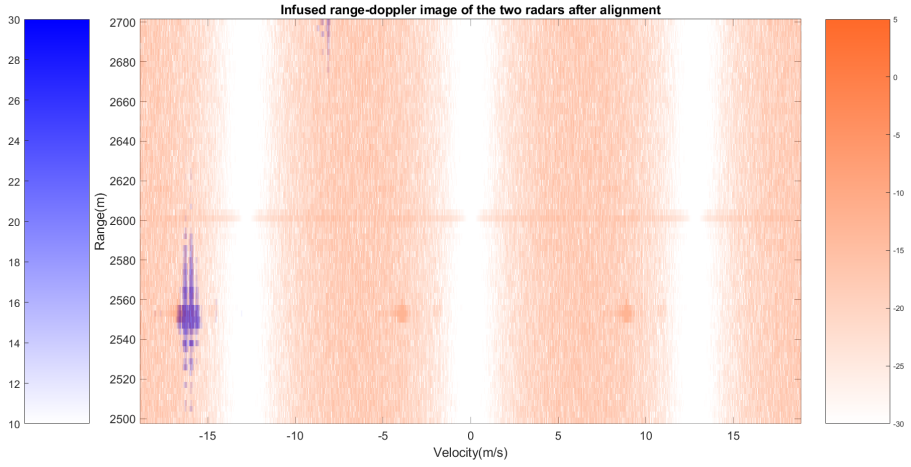

(b) Range-doppler figure after alignment

Figure 3.14: Infused range-Doppler figures of the two radars

The SSIM value explained in chapter 2, which calculates the similarity between two plots, was calculated using the figures before and after time alignment. The results before and after the data alignment are 0.88543 and 0.89143, respectively. As we can see, the SSIM value slightly increases by 0.006 after time alignment. Because the central part of the image is target-free, the change in SSIM value is not significant. However, the result is apparent in the infused PPI slow-time images.

3.6. CONCLUSION

This chapter used the cross-correlation method for temporal alignment of two independent radars' data; this procedure has been explained and tested with numerical simulation and actual data. The impact of several parameters on the estimation error was analyzed. The estimation with higher SNR, higher resolution, and relatively longer processing time would give a minor error. Moreover, the actual data was aligned in the temporal domain for two radars, and the targets coincide on the range-slow-time and range-Doppler plots.

4

VELOCITY AMBIGUITY RESOLVING

This chapter uses the data after alignment from the two radars to solve the velocity ambiguity. Some logic rules for fusing the data two radars have been developed and compared to find the most suitable one.

4.1. INTRODUCTION FOR SOLVING THE VELOCITY AMBIGUITY

Velocity ambiguity is a problem often encountered in pulse-Doppler radar measurement. Due to the periodicity of the transmitted pulse, waveforms with low pulse repetition frequency (PRF) will not be at the correct velocity position, called ambiguous velocity [42].

Current standard methods for solving the velocity ambiguity in pulse-Doppler radar detection are divided into two types [50]. One is to get the velocity by calculating the range differentiation when we have an accurate range measurement [24]. The other is to use multiple measurements with multiple PRFs to calculate the unambiguous velocity; the most well-known one is the Chinese Remainder Theorem [51].

This chapter will resolve the velocity ambiguity using the data from different radars and polarized channels. Some logic rules were applied to the data unfolded with the correct number of times to resolve the velocity ambiguity.

4.2. PROBLEM STATEMENT

The problem to be solved in this chapter is to do the data fusion from different radars and channels, develop different rules for the combination, and find the most suitable fusion rule to resolve the velocity ambiguity appearing in a single radar.

4.3. PROPOSED METHOD

4.3.1. DATA MODEL

A pulse-Doppler radar with wideband waveform is considered in this chapter, which is the same as the model for temporal alignment in chapter 3. The signature for a point-like

moving target can be expressed as [37]

$$\mathbf{T}_{ff,st}(l,m) = \frac{1}{K} e^{j2\pi f_D T_r m} e^{-j2\pi \frac{k_0}{K} l} e^{j2\pi \frac{v_0 T_r}{\delta R K} lm} \tag{4.1}$$

Where K is the number of range- cells, f_D is the doppler frequency, T_r is the sweep time, m is the slow time axis with M samples, k_0 is the corresponding range cell of the target, l is the range axis, v_0 is the velocity of the target, δR is range resolution.

However, most real targets are not point-like and have complex shapes, leading to their RCS variation with frequency, aspect angle, and polarization. Extended targets can be modeled as a linear combination of multiple scatterers taking into account the high range resolution of the radar. Then the $K * M$ matrix of the target's echo $\mathbf{Y}$ can finally become [37]:

$$\mathbf{Y} = \sum_{d=1}^{D} a_d * \mathbf{T}_{ff,st}(d) + \mathbf{n} \tag{4.2}$$

Where a_d is a complex amplitude, D is the number of scatters, $\mathbf{n}$ is the zero-mean Gaussian noise.

4.3.2. PROPOSED SOLUTION

Because the two radars have different central frequencies, they will have different unambiguous velocities. The maximum unambiguous velocity can be calculated by

$$v_a = \frac{\lambda}{2 * T_r} \tag{4.3}$$

Where v_a is the maximum unambiguous velocity, T_r is the PRI of the radar, λ is the wavelength of the radar. The output of the standard Doppler processing spans the velocity interval $[-v_a/2, v_a/2]$.

We can do joint processing of the two range-doppler data to resolve the velocity ambiguity taking advantage of the two radar's different unambiguous velocities. More precisely, the maximum unambiguous velocity for PARSAX is about 45m/s, the one for MESEWI is about 12m/s. Since the targets with velocity beyond unambiguous velocity will be folded to the velocity window of that radar, if we unfold the window of MESEWI, for example, three times, there will be three repeated targets in the plot with one at the proper velocity-range position, as the diagram in figure 4.1. It is easy to determine that the target with position coincides with the target position of PARSAX is the correct one.

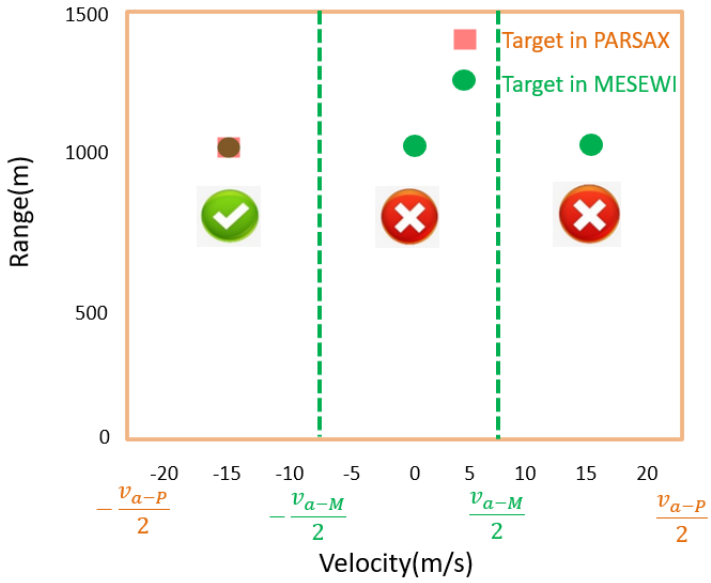

Figure 4.1: Velocity ambiguity diagram

Some detection rules can be developed to fuse different radars and channels using the principles explained above. The rules aim to keep the target at the proper position and discard some false alarms and targets with ambiguous velocity. Each rule will be implemented, and their results will be compared to choose the most suitable decision rule for this situation.

The decision rules are developed based on table 4.1. Different polarimetric channels of the same radar have the same ambiguous velocities. We set P_{HH} represents the detector output of PARSAX's HH channel, P_{VV} represents the detector output of PARSAX's VV channel. The same for M_{HH} and M_{VV} of MESEWI. For each cell, when P_{HH} (or P_{VV},M_{HH},M_{VV}) equals to 1, there exists a target in this channel. Otherwise, the value will be zero. We have in total four channels, HH and VV channels for PARSAX and MESEWI. The cross-polarimetric channels of both radars are not used for processing, as they typically have lower power[14]. We can check if the target is detected at each correct location of this target. For rule 1, if the target is detected in at least three channels, we assume the target is detected. Otherwise, we consider there is no target. For rule 2, if the target is detected in at least two channels from different radars, we give a positive detection output. By traversing each cell in the detector output matrix of each channel, we can get the logic output based on each rule.

number	Rule
1	$(P_{HH} + P_{VV} + M_{HH} + M_{VV}) \geqslant 3$
2	$(P_{HH} \wedge M_{HH}) \vee (P_{HH} \wedge M_{VV})$ $\vee (P_{VV} \wedge M_{HH}) \vee (P_{VV} \wedge M_{VV})$

Table 4.1: Logic rule table

4.4. NUMERICAL SIMULATION

4.4.1. SIMULATION SET UP

The range resolution for the two radars in this simulation is both 3 meters. Here we consider several targets that have separated scatters.

A full polarimetric radar is considered in this chapter, which means one radar has several channels with different polarization(HH, HV, VH, VV). Here we simulate the results for HH and VV channels. The relationship between the transmitted and received signal is in equation 4.4 [22].

$$\begin{pmatrix} \mathbf{E}_H^R \\ \mathbf{E}_V^R \end{pmatrix} = \begin{pmatrix} S_{HH} & S_{VH} \\ S_{VH} & S_{VV} \end{pmatrix} \begin{pmatrix} \mathbf{E}_H^T \\ \mathbf{E}_V^T \end{pmatrix} \tag{4.4}$$

where $\mathbf{S} = \begin{pmatrix} S_{HH} & S_{VH} \\ S_{VH} & S_{VV} \end{pmatrix}$ is the complex back scattering matrix and $\mathbf{E}^T$, $\mathbf{E}^R$ represent the transmitted and received electric field strength of the signal. In this simulation, the scattering matrix is defined for each scatter.

Then the reflection intensity value of one target can be calculated using equation 4.5.

$$I = \mathbf{S}_1 e^{-j2\pi \frac{R_1}{\lambda}} + \mathbf{S}_2 e^{-j2\pi \frac{R_2}{\lambda}} + \ldots + \mathbf{S}_n e^{-j2\pi \frac{R_n}{\lambda}} \tag{4.5}$$

Where n is the number of scatters, $\mathbf{S}_n$ is the complex back-scattering matrix for the nth scatter, R_n is the range of the n-th scatter, λ is the wavelength of the radar.

The $\mathbf{S}_n$ for each scatterer can be modeled as

$$\mathbf{S}_n = \begin{bmatrix} e^{j\phi} & 0 \\ 0 & \beta e^{-j\psi} \end{bmatrix} \tag{4.6}$$

where ϕ and ψ are random number belong to $[0, 2\pi]$, β is the radio between HH channel and VV channel.

An example of the RCS fluctuating with the change of frequency can be seen in figure 4.2. The RCS could be very different with the different settings of β and amplitude and seeing into a different frequency.

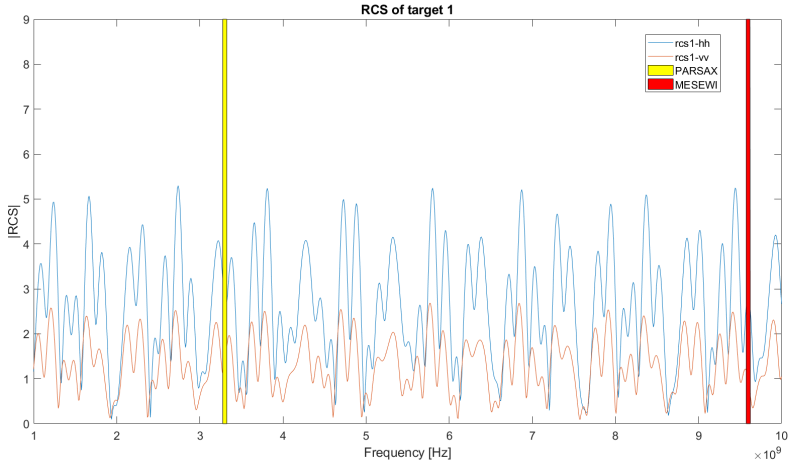

(a) RCS1

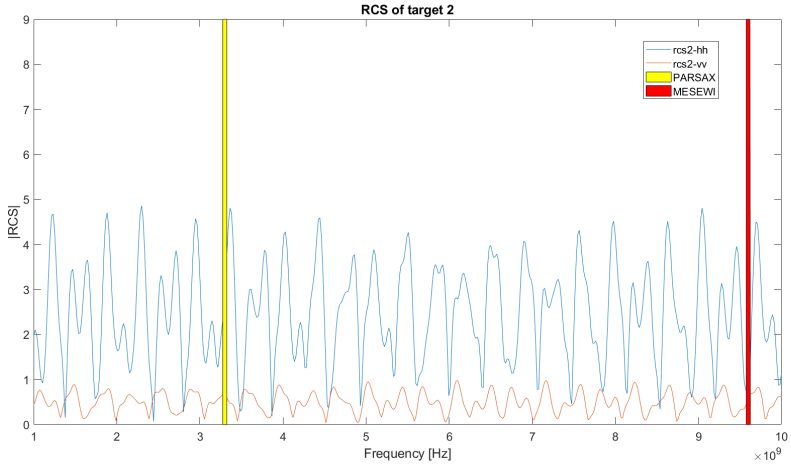

(b) RCS2

Figure 4.2: RCS fluctuating of the targets

Since the target length is set within the range resolution of the radar, the target echo can be calculated using equation 4.1. For each target, combining equation 4.1 4.5 and 4.6, the reflected signal can be expressed as

$$\boldsymbol{Y} = \alpha \cdot I \cdot \mathbf{T}_{ff,st} + \mathbf{n} \tag{4.7}$$

where $\mathbf{n}$ is a zero mean Gaussian noise.The parameter α is the signal to noise ratio with other parameters that have a mean power of 0dB .

4.4.2. SIMULATION RESULT

The procedure of the simulation follows the items below:

a) Set the radar parameters

The two radars have been set that have the same center frequency as PARSAX and MESEWI; the parameters for these two radars are listed in table 4.2.

	PARSAX	MESEWI
Range resolution [m]	3	3
Central frequency [GHz]	3.3	9.6
Bandwidth [MHz]	50	50
PRI [ms]	1	0.61

Table 4.2: Parameters of radars

b) Generation of target echo signal

Using the reflected signal model from the target in equation 4.1 and 4.2, five echos of the moving targets have been created, the range and velocity of these targets are listed in table 4.3.

Target	Range(m)	Velocity(m/s)
1	1000	-30
2	1200	10
3	1050	-15
4	950	-18
5	750	25

Table 4.3: Moving target information

The ratio between the back-scattering amplitude of the HH channel and VV channel β has been set to 0.3. The number of range cells K equals 512, and the number of Doppler cells M is 128. The signal-to-noise ratio is 25dB per scatterer. The echo of each target can be created using the data model in section 4.4.1.

c) Apply fast coherent integration explained in chapter 3.

Hamming window has been applied to the range and doppler domain to suppress the sidelobes. After fast CI, the data of MESEWI is unfolded seven times, and the data of PARSAX is unfolded three times.

d) Apply CFAR detector in each doppler cell

The number of training cells is 20, and the number of guard cells is 2. The probability of false alarm in this simulation is as 10^{-5}.

e) Apply logic to the CFAR output of the 4 channels

Before applying the logic rules, the velocity window of MESEWI should be cut to the same range of velocity with PARSAX; then, it will be interpolated to the velocity axis of PARSAX. After this, the data from different channels can be added to apply different logic rules.

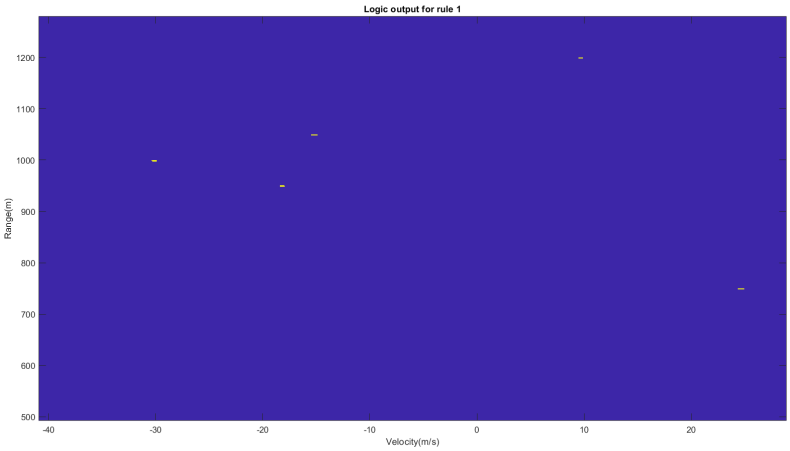

(a) Logic output of rule 1

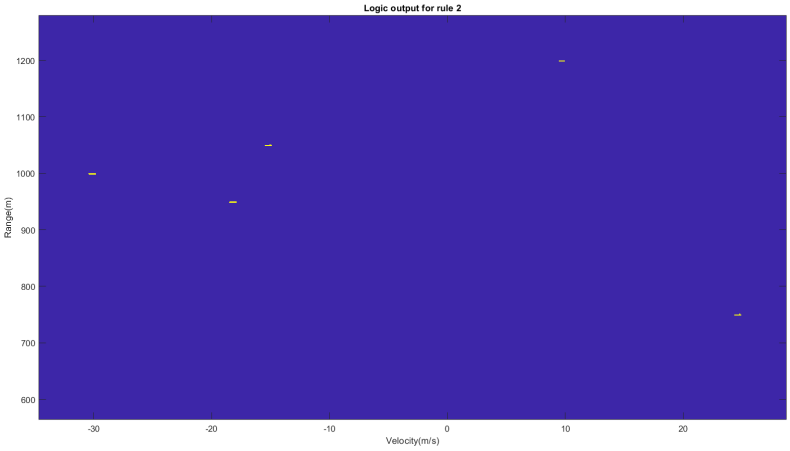

(b) Logic output of rule 2

Figure 4.3: Logic output

f) Calculate the probability of full detection and correct detection

Considering one target may occupy more than one cell, the probability of detection for a single target is the probability of declaring the presence of the target within a gate around its correction position [37]. If we set the position of the target in the detection output is (v, r), the true position of the target is (v_0, r_o), if

$$(|v - v_0| \leqslant \delta v) \wedge (|r - r_0| \leqslant \delta R) \tag{4.8}$$

then we declare that it is the correct detection. For multiple targets' scenario, like in this project, the probability of full detection P_{fd} is the ratio between the number of detected targets and the total number of targets in the radar scan range.

The probability of correct detection is the probability to have all the targets detected in its right position and no false alarms appears. In equation 4.9, the N_{FA} represents the number of false alarms.

$$(P_{fd} = 1) \wedge (N_{FA} = 0) \tag{4.9}$$

The performance of these logic rules can be evaluated after 100 times Monte-Carlo simulations for each SNR; the result curves are shown below.

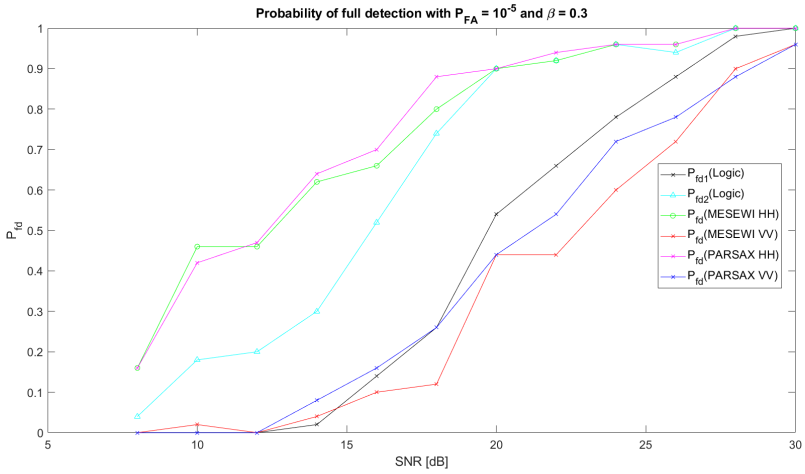

(a) Probability of full detection of single channels and logic outputs vs. SNR of 5 targets, $P_{fa} = 10^{-5}$

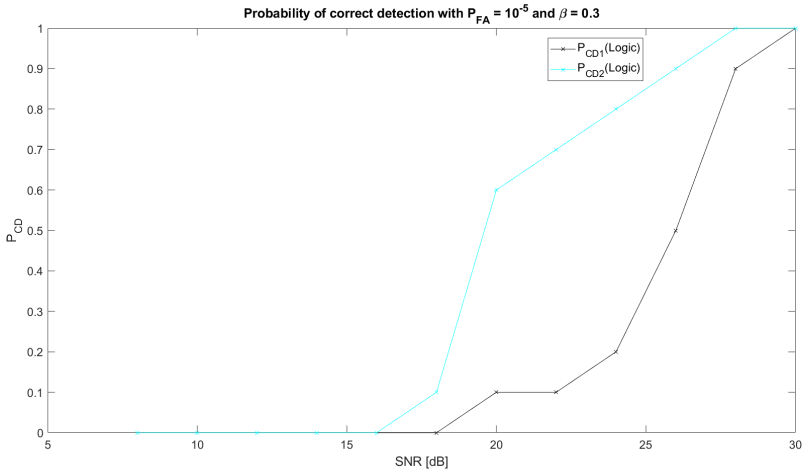

(b) Probability of correct detection after applying the two logic rules vs. SNR of 5 targets, $P_{fa} = 10^{-5}$

Figure 4.4: P_{fd} and P_{cd} curve for multiple targets with $\beta = 0.3$

In figure 4.4(a), we can see the probability of full detection of logic rule 2 has a better performance than logic rule 1 because it can discard the VV channels, which have a worse detection performance. Below 20dB, the values of P_{fd} for the two radars' HH channels have a slightly better performance than the logic output of rule 2, this is because the detected targets in the two radars may not fully overlap, which causes the detection loss in data fusion. Moreover, since the ratio between the VV channel and HH channel is set to 0.3, we can see that the P_{fd} value of the HH channel go over 0.5 at around 12dB SNR, and the one for the VV channel exceeds 0.5 at around 22dB SNR,

which means this radio causes about 10 dB loss of SNR, which agreed with the simulation, as 20log10(0.3)= -10dB.

More importantly, since our goal is to solve the velocity ambiguity, the probability of correct detection is an important parameter to evaluate the feasibility of the proposed method. We have simulated some targets whose velocity is above the maximum unambiguous velocity of PARSAX, which means that because of velocity ambiguity, all P_{CD} values for single channels would be zero. However, in figure 4.4(b), we can see that the logic output has a desirable P_{CD} value, sometimes even close to 1, which means using the logic rules to fuse data from different channels provide good performance for velocity ambiguity resolving. Moreover, the logic output of rule 2 has a better performance than logic rule 1. Therefore, selecting the data from at least two channels from different radars is enough to solve the velocity ambiguity, and it is the more suitable way for dual-polarization and multi-frequency data fusion.

To investigate the influence of the ratio between the HH channel and VV channel, different values of β were chosen. The resulting curves after 100 trials Monte-Carlo simulation with $\beta = 0.1$ and $\beta = 0.5$ are shown below.

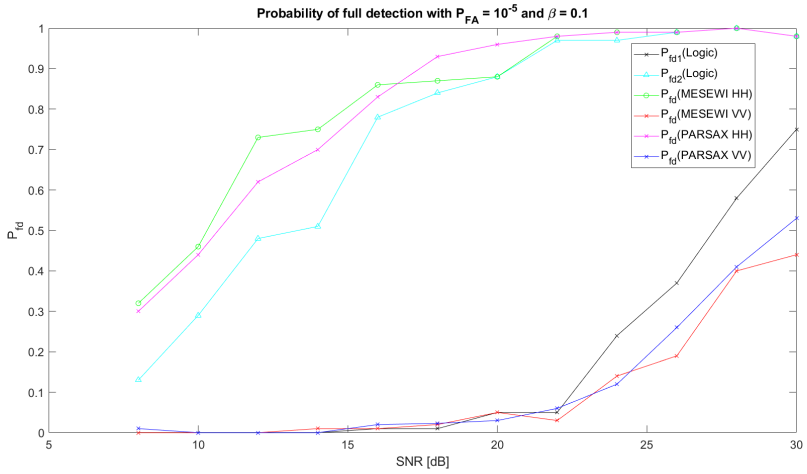

(a) Probability of full detection of single channels and logic outputs vs. SNR of 5 targets, $P_{fa} = 10^{-5}$

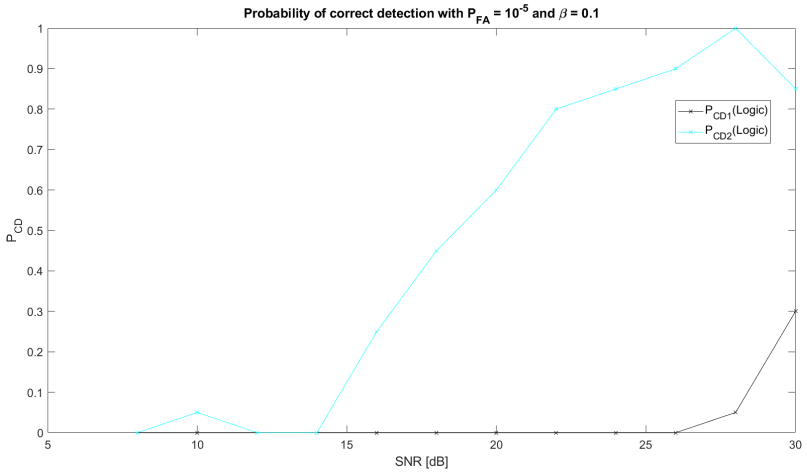

(b) Probability of correct detection after applying the two logic rules vs. SNR of 5 targets, $P_{fa} = 10^{-5}$

Figure 4.5: P_{fd} and P_{cd} curve for multiple targets with $\beta = 0.1$

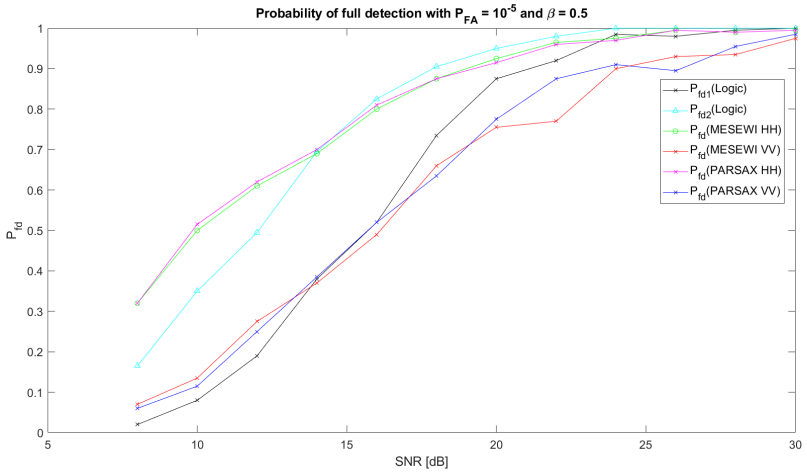

(a) Probability of full detection of single channels and logic outputs vs. SNR of 5 targets, $P_{fa} = 10^{-5}$

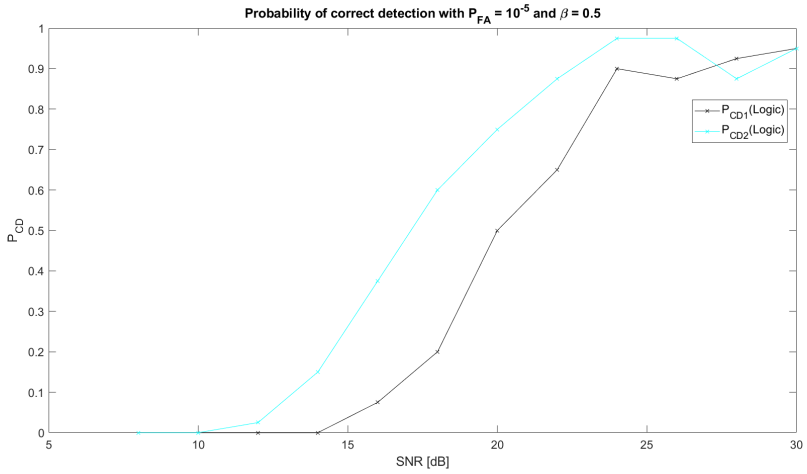

(b) Probability of correct detection after applying the two logic rules vs. SNR of 5 targets, $P_{fa} = 10^{-5}$

Figure 4.6: P_{fd} and P_{cd} curve for multiple targets with $\beta = 0.5$

From the curves above, we can see that the changing of valve β does not have much influence on the performance of the logic 2 rule, this is because only by fusing the channel with more substantial power in both radars could work, the power change of the weak channel would not have an impact on the output of logic 2. However, since logic rule 1 needs at least three channels from the radars, one weak channel will exist. When the power of this weak channel decreases, the performance of logic rule 1 would be worse.

4.5. CONCLUSION

In this chapter, two rules of fusing the radar data in different radar and polarized channels have been proposed and tested with simulation; these rules can be used to resolve the velocity ambiguity of the moving target. The simulation result shows that the proposed logic rule 2, which fuses minimal two channels from different radars, has a better detection performance than fusing data from at least three channels. Furthermore, it would not be influenced by the ratio of the power of different polarimetric channels, which means it is a more suitable way to combine the data from different channels. Moreover, logic rule two can compensate for the weak channels and give a good performance in the probability of correct detection, which means the velocity ambiguity in a single channel could be resolved.

5

TARGET TRACKING AND FEATURES EXTRACTION

This chapter used the aligned and fused data to do the target tracking and range signature extraction. The results from the previous chapters are combined in this chapter; the spatial offset and time offset results were used to align the data; the logic rule in chapter 4, which fuses the four channels, and applying the Kalman filter to do the single target tracking. Then the tracking procedure was implemented on actual data.

5.1. INTRODUCTION

Typical multiple measurement tracking methods like probability associated filter [4] merge the hypothesis from each measurement. When coming to multi-channel target tracking, it is often a multiple measurement target tracking problems. Typical multiple measurement tracking methods like probability associated filter [4] merge the hypothesis from each measurement. The study [13] compared two methods used for Kalman filter-based multi-sensor data fusion. The first method merges the multi-sensor data through the observation vector of the Kalman filter, whereas the second one combines the multi-sensor data based on a minimum-mean-square-error criterion. In [1], the State Vector Fusion (SVF), Measurement Fusion (MF) and Gain fusion (GF) are implemented in the tracking system. These all are valuable methods in the multiple measurement target tracking areas.

Nevertheless, in this project, we have already fused the data from the four channels to resolve the velocity ambiguity, and this fusion rule could give the probability of correct detection close to 1 at high SNR; this led to the idea of using the fused logic output as the measurement and doing target tracking based on this measurement with highly accurate range and Doppler information. Therefore, the logic output from chapter 4 would be used to do the single measurement target tracking in this chapter. The field of target tracking has been extensively studied over the decades. Some classical filters, like Kalman filter[8], Particle filter [36] and IMM filter [20] have been used for tracking with a

single stream of measurements.

When facing multiple target situation, targets should be well recognized and classified .There are two feature vectors used for radar target classification: scattering center and complex natural resonance (CNR) frequency [23]. Scattering center were used in researches based on feature extraction methods like Programming (EP)-based CLEAN algorithm [10], model-based technique (LS-based Prony) and the Fast Fourier Transform (FFT)-based CLEAN algorithm[19]. The authors in [43, 30, 49] use the CNR frequency for the classification. The method in this chapter refers to the principle of scattering center and uses the tracking result to do the feature extraction.

5.2. PROBLEM STATEMENT

The problems to be solved in this chapter are listed below.

- Use the fused measurement from logic rule to do target tracking.

- Extract range signature of the target.

5.3. PROPOSED SOLUTION

From the simulation results in chapter 4, rule 2, which fuses a minimum of two channels from different radars, is more suitable for the data fusion. Therefore, this logic rule would be used to combine the channels in this chapter. Since the frame length of the two radars is different because of different PRI, like it is shown in figure 5.1, we can set the duration of PARSAX as the measurement interval and choose a certain number of pulses in MESEWI, based on these pulses we can have the same duration as PARSAX. Two-dimensional FFT would be applied to the PARSAX and MESEWI data with the same duration. After doing detection on the range-Doppler data and applying logic to resolve the velocity ambiguity, the CFAR output of the logic can be obtained for this time interval, which is the measurement of range and velocity at this time. The measurement at each time step can be used for the tracking procedure.

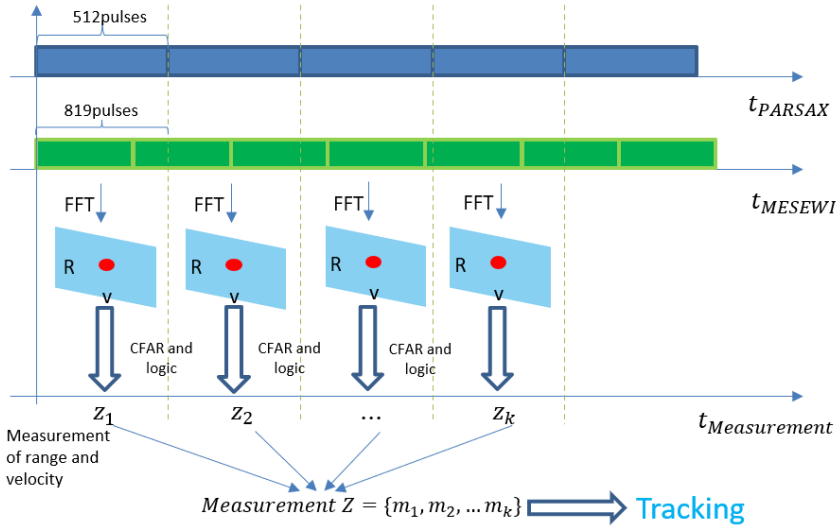

Figure 5.1: Diagram of tracking method

For linear and Gaussian distributed problems, the Kalman filter is optimal for target tracking. Therefore, the filter used in this chapter is the Kalman filter. The Kalman filter's working procedure [44]is explained below.

5.3.1. DYNAMIC MODEL

The Kalman filter for tracking moving objects estimates a state vector representing the parameters of the target, such as position and velocity, based on a dynamic/measurement model. This chapter deals with a typical second-order one-dimensional Kalman filter tracker whose actual state vector is defined as

$$\mathbf{x}_k = (x_k, v_k)^T \tag{5.1}$$

Where x_k and v_k are the proper position and velocity of the target moving object, respectively. Superscript $(\cdot)^T$ denotes vector/matrix transpose. The dynamic model for this chapter is a constant velocity (CV) model. The dynamic of the system can be expressed as

$$\mathbf{x_{k+1}} = \mathbf{F x_k} + \mathbf{w_k} \tag{5.2}$$

where $\mathbf{x_k}$ is the state vector at time step kT, T is the time interval between the frames. $\mathbf{w_k}$ is the processing noise and $\mathbf{w_k} \sim \mathscr{CN}(\mathbf{0}, \boldsymbol{Q})$. $\mathbf{F}$ is the transition matrix relating the previous time step $k-1$ to the current state k, which is expressed as

$$\mathbf{F} = \begin{bmatrix} 1 & T \\ 0 & 1 \end{bmatrix} \tag{5.3}$$

5.3.2. MEASUREMENT MODEL

The measurement model of the system is

$$\mathbf{z_k} = \mathbf{H}\mathbf{x_k} + \mathbf{y_k} \tag{5.4}$$

where $\mathbf{z_k}$ is the measurement vector, $\mathbf{H}$ is the measurement matrix, $\mathbf{y_k}$ is the observation noise and $\mathbf{y_k} \sim \mathscr{CN}(\mathbf{0}, \boldsymbol{R})$. The Position-velocity-measured (PVM) system assumes that the sensor system can measure position and velocity simultaneously. One example of the PVM model system is a pulse-Doppler radar. The PVM model can also express sensor fusion systems using communications of position/velocity sensors. $\mathbf{H}$ of this model is expressed as

$$\mathbf{H} = \begin{bmatrix} 1 & 0 \\ 0 & 1 \end{bmatrix} \tag{5.5}$$

5.3.3. TARGET TRACKING WITH KALMAN FILTER[44]

The Kalman filter tracker sequentially estimates the state vectors via the Kalman filter equations based on the abovementioned models. The prediction and estimation are calculated as

$$\widetilde{\mathbf{x}}_k = \mathbf{F}\widehat{\mathbf{x}}_{k-1} \tag{5.6}$$

$$\widehat{\mathbf{x}}_k = \widetilde{\mathbf{x}}_k + \mathbf{K}_k(\mathbf{z}_k - \mathbf{H}\widetilde{\mathbf{x}}_k) \tag{5.7}$$

where predicts and estimates are denoted by $\widehat{\mathbf{x}}_k$ and $\widetilde{\mathbf{x}}_k$, respectively. $\mathbf{K}_k$ is the Kalman gain that minimizes the errors in the estimated position and velocity, and it can be calculated via

$$\mathbf{K}_k = \widetilde{\mathbf{P}}_k\mathbf{H}^T(\mathbf{H}\widetilde{\mathbf{P}}_k\mathbf{H}^T + \mathbf{R}) \tag{5.8}$$

where $\widetilde{\mathbf{P}}_k$ is the covariance matrix of errors derived from

$$\widetilde{\mathbf{P}}_k = \mathbf{F}\widehat{\mathbf{P}}_{k-1}\mathbf{F}^T + \mathbf{Q} \tag{5.9}$$

$$\widehat{\mathbf{P}}_k = \widetilde{\mathbf{P}}_k - \mathbf{K}_k\mathbf{H}\widetilde{\mathbf{P}}_k \tag{5.10}$$

Moving object tracking obtains an accurate and sequential estimation of the target position and velocity by using equations 5.7–5.10.

5.3.4. K-MEANS CLUSTERING

Since the logic output of one target may cover several pixels, to avoid missing information and improve the final result, K-means clustering [3] was used in this procedure.

The k-means++ algorithm uses a heuristic to find centroid seeds for k-means clustering.

The k-means algorithm chooses seeds as follows, assuming the number of clusters is k.

a) Select an observation uniformly at random from the data set, X. The chosen observation is the first centroid, and is denoted c_1.

b) Compute the distances from each observation to c_1. Denote the distance between c_j and the observation m as $d(x_m, c_j)$.

c) Select the next centroid, c_2 at random from X with probability

$$\frac{d^2(x_m, c_1)}{\sum_{j=1}^{n} d^2(x_j, c_1)} \tag{5.11}$$

d) To choose center j:

Compute the distance from each observation to each centroid, and assign each observation to its closest centroid. For $m = 1, ..., n$ and $p = 1, ..., j–1$, select centroid j at random from X with probability

$$\frac{d^2(x_m, c_p)}{\sum_{h; x_h \in c_p} d^2(x_h, c_p)} \tag{5.12}$$

where C_p is the set of all observations closest to centroid c_p and x_m belongs to C_p. Select each subsequent center with a probability proportional to the distance from itself to the closest chosen center. Repeat step d until k centroids are chosen, which is the position of the range and velocity of each target.

5

5.4. NUMERICAL SIMULATION

The target model used in this chapter is the same as the one in chapter 4, in which four polarized channels from the two radars are generated. For simplification, only one target is considered in this simulation to do the tracking.

The procedure of the simulation follows the items listed below:

a) Set the radar parameters

The two radars in the simulation have been set to have the same center frequency as PARSAX and MESEWI; the parameters for these two radars are listed in table 5.1.

	PARSAX	MESEWI
Range resolution [m]	3	3
Central frequency [GHz]	3.3	9.6
Bandwidth [MHz]	50	50
PRI [ms]	1	0.61
SNR [dB]	28	20

Table 5.1: Parameters of radars

b) Generation of target echo signal

Using the reflected signal model from the target in equation 4.1 and 4.2, the echo of the moving target has been created, the range and velocity of the target is in table 5.2.

Target	Range(m)	Velocity(m/s)
1	1000	-30

Table 5.2: Moving target information

The trajectory of the target can be seen after applying IFFT in the fast time domain. The results are shown in figure 5.2. Hamming window has been applied to both fast-time and slow-time dimensions to suppress the sidelobes.

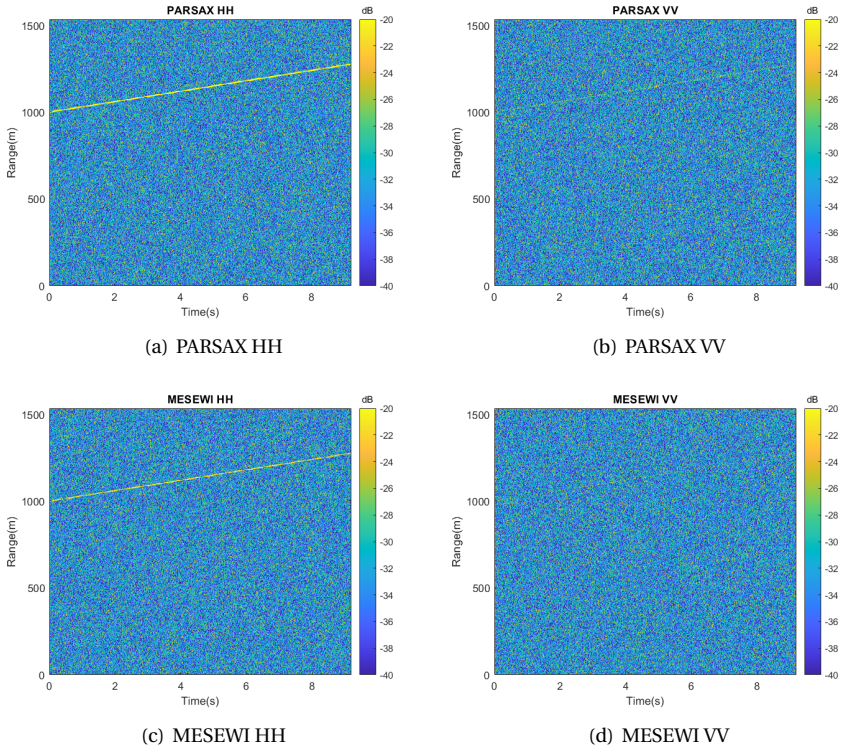

(a) PARSAX HH (b) PARSAX VV

(c) MESEWI HH (d) MESEWI VV

Figure 5.2: Range-Doppler image of the two radars

c) Create Range-Doppler image of each channel

The FFT along slow time has been applied to each frame. In this simulation, the number of pulses in each time frame is 419 for MESEWI and 256 for PARSAX; the time step duration is 0.255s; after applying fast coherent integration mentioned in Chapter 3, we can get the range-Doppler data matrix of each channel within each frame.

d) Apply CFAR detector to each channel

We use the Cell-averaging CFAR detector to do the detection. The number of training cells is 40, and the number of guard cells is 4. The probability of false alarm is set as 10^{-8}. The CFAR detection is applied to each Doppler cell.

e) Apply logic rule to the output of the detector

The logic rule fuses minimal two channels from two different radars. After applying this logic to resolve velocity ambiguity, the output of one frame is shown in figure 5.3. It is clear that after data fusion, the target's position is correct at each time step.

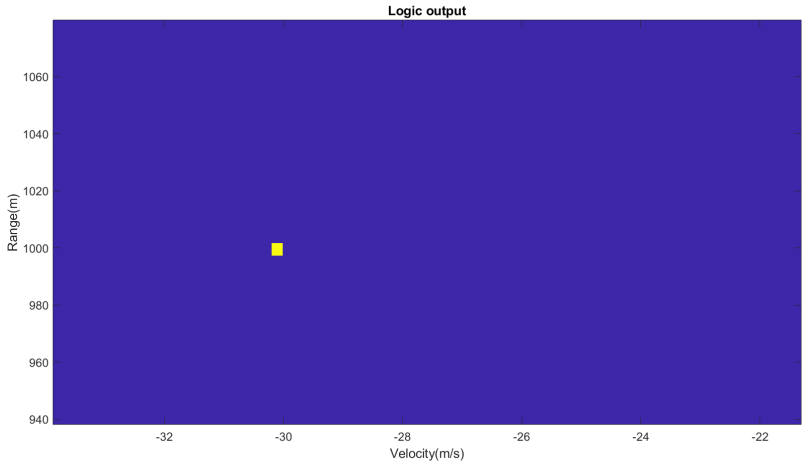

Figure 5.3: Logic output of the 4 channels

f) Using Kalman filter to do the tracking

After applying K-means clustering, the measurement of the target's range and velocity value can be obtained from the logic output. According to the velocity measurement at each time step, the target is assumed to have a constant velocity, so the state transition matrix for the CV model was used. Then the measurements at each time step were used to do the Kalman filter-based target tracking.

The choice of the parameters of the Kalman filter to get a satisfactory output is a complicated problem. Usually, one assumes an initial position according to the measurement value. For the chosen of the variance in dynamic model **Q** and variance in measurement model **R**, usually one assumes an initial value for **Q** and **R** in the filter[32], which could be close to zero and later adaptively update and estimate it. The value of Q and R are 2 and 0.01.

The results of the filter output are shown below.

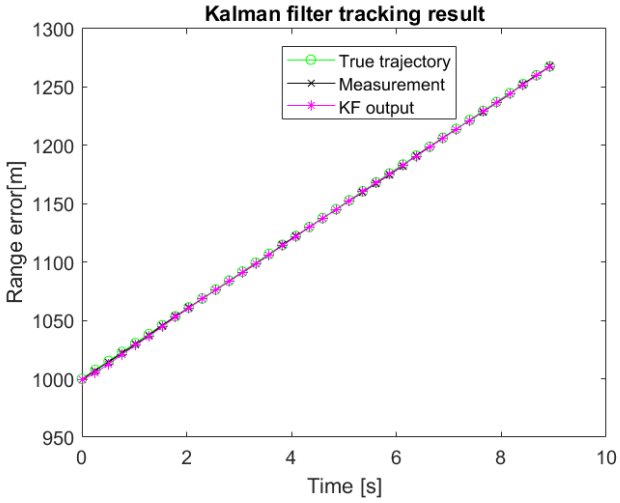

Figure 5.4: Kalman filter tracking output

As shown in figure 5.4, the measurement trajectory and the tracking output are pretty close to the actual trajectory, which means this method could work properly. The tracking and measurement error at each time step is shown in figure 5.5. 3-sigma Cramer Rao Bound [32] was chosen to evaluate the uncertainty of the filter. In the figure, we can see the bound convergence within the range resolution after the tracking procedure, which is satisfactory.

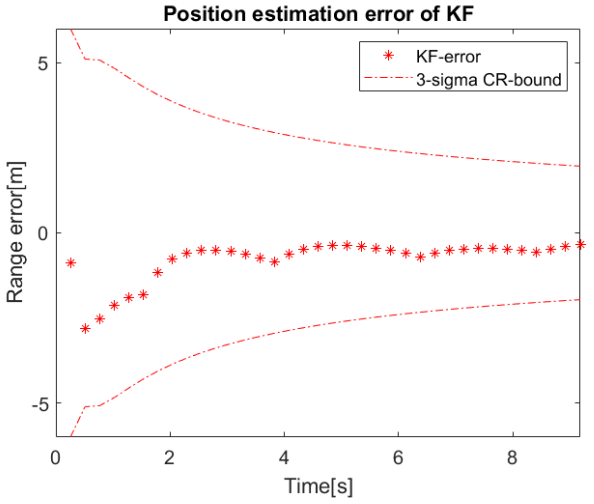

Figure 5.5: Kalman filter tracking error

The target's velocity is -30m/s, which is over the maximum unambiguous velocities

of PARSAX and MESEWI; this would cause incorrect velocity estimation in the tracking procedure of a single radar which results in a wrong trajectory of the target. Therefore, fusing the data with frequency and polarization diversity could improve the tracking performance.

Now consider a constant velocity target whose trajectory is not directed towards the radar. There is an angle between the trajectory and the radial line of the radar beam. A diagram of this is shown in figure 5.6.

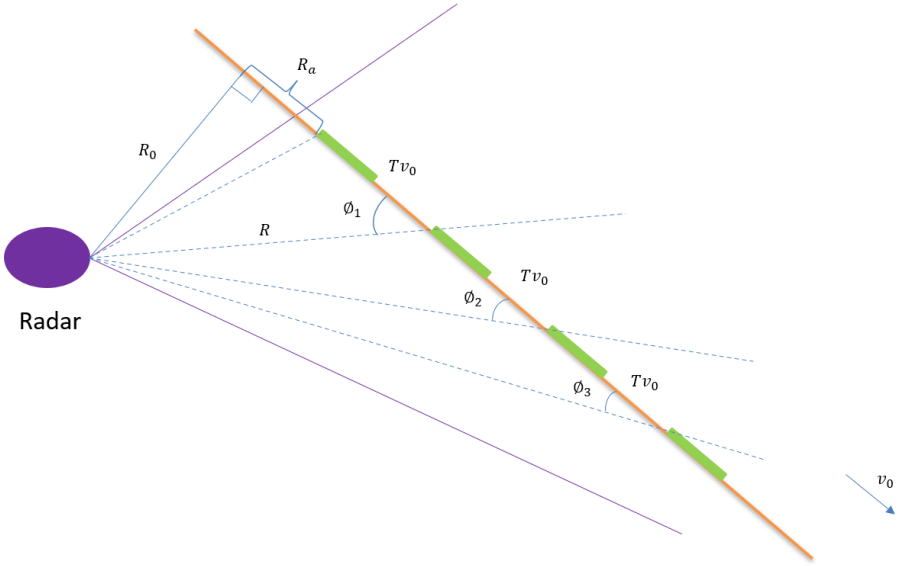

Figure 5.6: Diagram of the target trajectory

Where R_0 is the distance perpendicular from the radar to the target's trajectory, v_0 is the true velocity. The angle ø is the target aspect angle which changes with time and thus targets RCS changes. We define the duration of each time step is T, K is the kth time step, then at time kT, the relative range of the target is $R = \sqrt{R_0^2 + (R_a + v_0 kT)^2}$. Since the target has a constant velocity, the relative velocity of the target at each time step is $v_0 cos\emptyset_k$.

In this simulation, $v_0 = -30m/s$, $R_0 = 1000m$,$R_a = 200m$, $T = 0.255s$.

Using the target RCS model explained in chapter 4, the reflection intensity value of one target can be calculated using equation 5.13.

$$I = \mathbf{S}_1 e^{-j2\pi \frac{R_1}{\lambda}} + \mathbf{S}_2 e^{-j2\pi \frac{R_2}{\lambda}} + ... + \mathbf{S}_n e^{-j2\pi \frac{R_n}{\lambda}} \tag{5.13}$$

Where n is the number of scatters, $\mathbf{s}_n$ is the complex back-scattering matrix for the nth scatter, R_n is the range of the nth scatter, λ is the wavelength of the radar.

The $\mathbf{S}_n$ for each scatterer can be modeled as

$$\mathbf{S}_n = \alpha_n \begin{bmatrix} e^{j\phi} & 0 \\ 0 & \beta e^{-j\psi} \end{bmatrix} \tag{5.14}$$

where ϕ and ψ are random number belong to $[0, 2\pi]$, β is the radio between HH channel and VV channel, α_n is the amplitude of the scatter.

The information of the scatters of this target are listed in table 5.3.

	Range [m]	α	ϕ	ψ
scatter 1	R	0.8	$\frac{\pi}{3}$	$\frac{\pi}{4}$
scatter 2	R+5.1	0.2	$\frac{\pi}{2}$	$\frac{\pi}{2}$
scatter 3	R+15.3	0.3	$\frac{\pi}{6}$	$\frac{\pi}{2}$
scatter 4	R+10	0.7	$\frac{\pi}{8}$	$\frac{\pi}{3}$

Table 5.3: Scatter information of the target

The radio between HH channel and VV channel β in this simulation is 0.5, SNR is 18dB. The range signature of the target of each channel with the changing of Φ can be seen in figure 5.7.

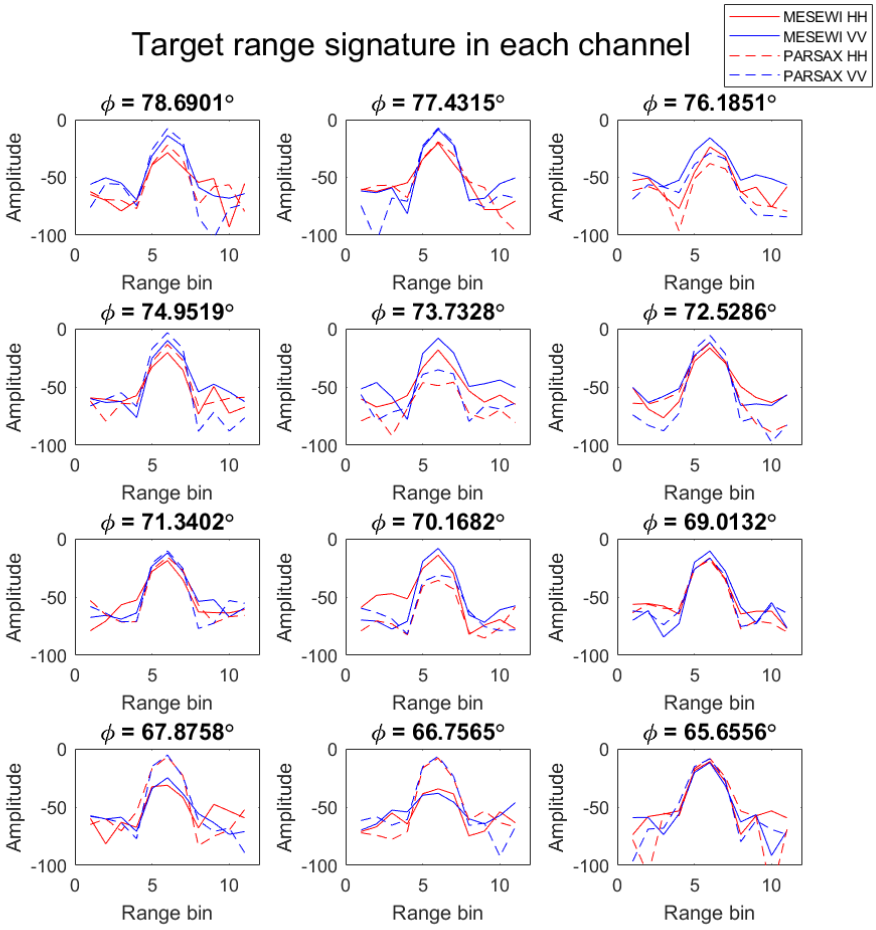

Figure 5.7: Range signature of the target

The range signature of the target fluctuates with the changing of aspect angle. At some point, there is a 30dB difference in the absolute value of the amplitude. In this simulation, the frequency diversity(from different radars) causes more fluctuation than the polarimetric diversity(from the different polarized channels).

5.5. EXPERIMENTAL VALIDATION

The experimental data used for this validation is the highway data of N470 collected on 29th June 2021, the same as the data used in chapter 3, time alignment. Using the estimated cable length of PARSAX equal to 36m obtained in chapter 2 and MESEWI's time shift of 0.89s obtained in chapter 3, the data is aligned.

For simplification, single-target tracking is applied to the data. Since there are many

targets on the highway, to prevent confusion with other targets, a specific range of distance from the radar was chosen, like it is shown in figure 5.8.

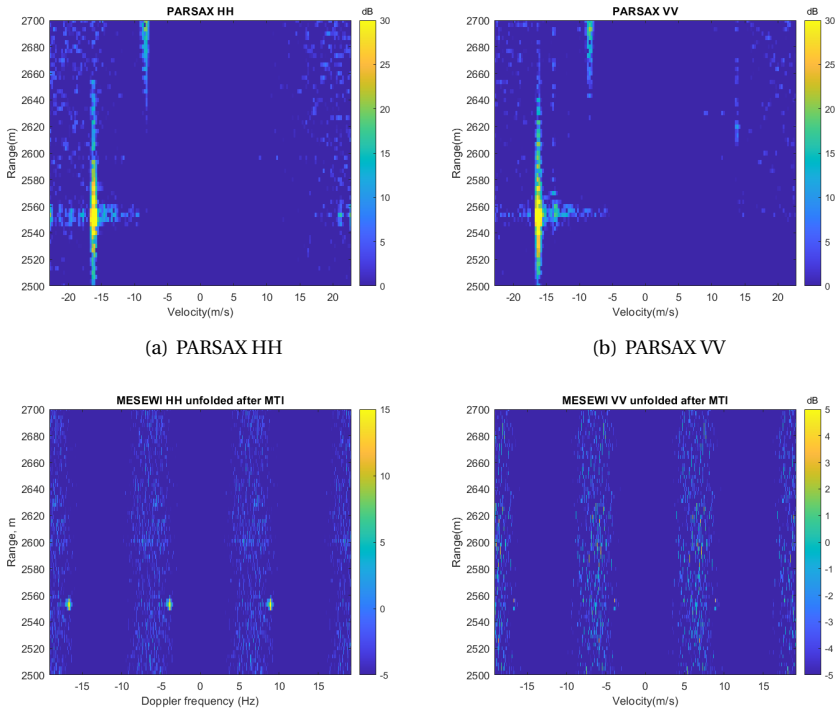

(a) PARSAX HH

(b) PARSAX VV

(c) MESEWI HH

(d) MESEWI VV

Figure 5.8: Range-Doppler image of target 1 of the two radars

Because the size of the two radars' data is different, they should first be interpolated to the same size and then do the following processing. A cell-averaging CFAR detector has been applied to these channels, with 20 training cells and two guard cells. The false alarm rate, in this case, is 1e-8. The CFAR output of the four channels is shown in figure 5.9.

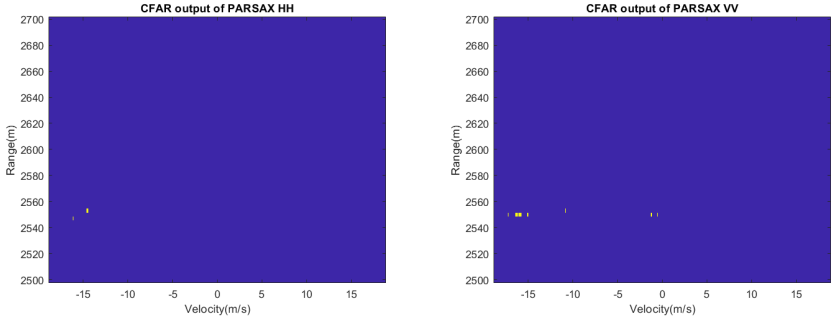

(a) CFAR output of PARSAX HH

(b) CFAR output of PARSAX VV

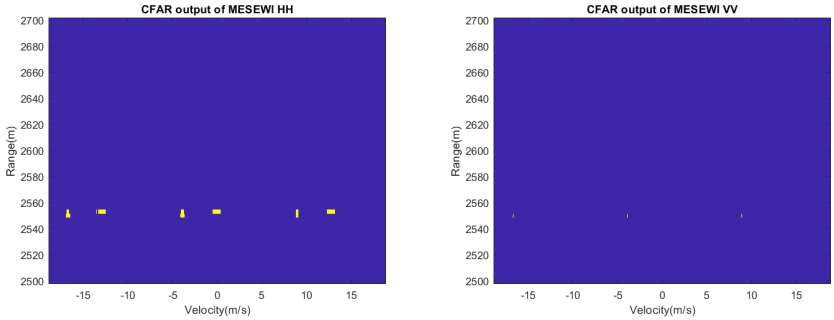

(c) CFAR output of MESEWI HH

(d) CFAR output of MESEWI VV

Figure 5.9: CFAR output of the two radars of target 1

After applying the logic rule of fusing the four channels' data to resolve velocity ambiguity, the output of one frame is shown in figure 5.10.

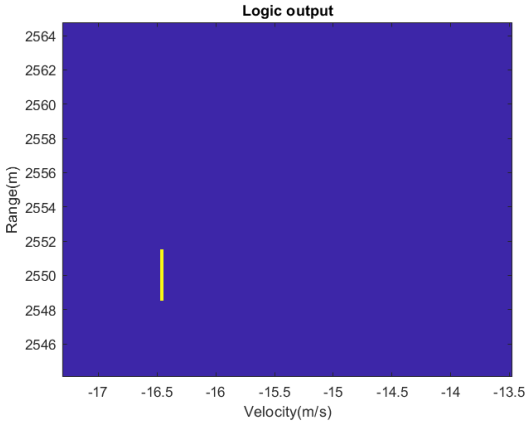

Figure 5.10: Logic output of target 1 from four channels(experimental data)

From this output, after applying K-means clustering, the measurement of the target's range and velocity value can be obtained; then, we collect the measurement at each time step. According to the velocity measurement at each time step, the target is assumed to have a constant velocity of $-15 m/s$, so the state transition matrix for the CV model was used.

The result after applying the Kalman filter is shown below.

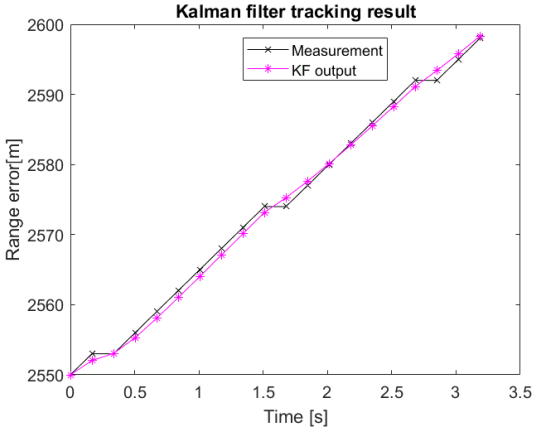

Figure 5.11: Filter output of target 1

The tracking offset compared to the measurements at each time step can be seen in figure 5.12.

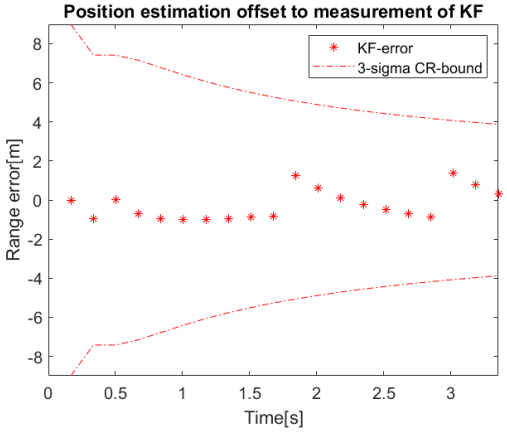

Figure 5.12: Tracking offset of target 1

The tracking results of the velocity and range estimation at each time step could be used to extract the target's signature. The signatures in different channels are different. The changing of the target's signature with time step is shown in figure 5.13.

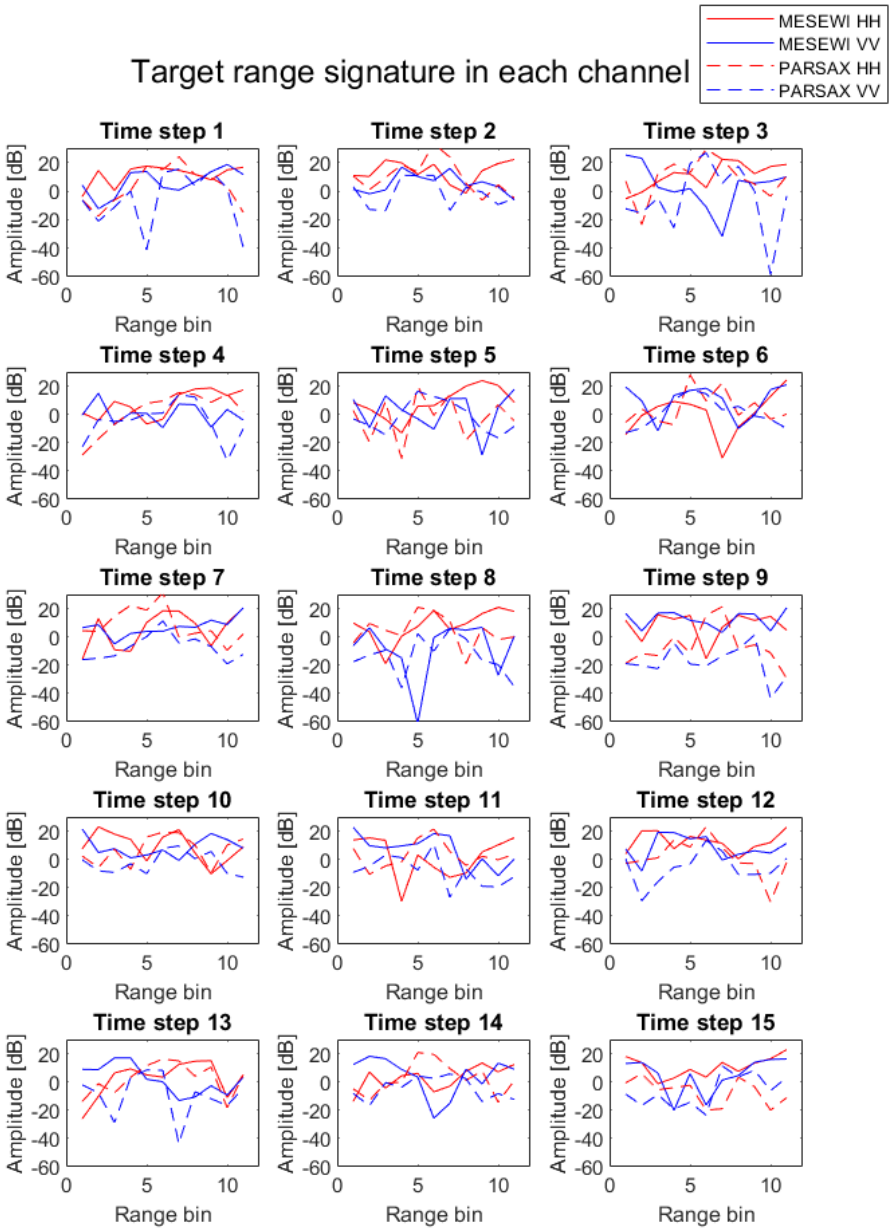

Figure 5.13: Range signature of target 1(real data)

It can be seen in 5.13 that the shape of the target responses has some recognizable

features over time. Thus for target 1, there are several time frames in which strong reflectors are present in the close and in the far side of the target, which determines the range extent of this target.

In order to prove the adaptability of the method, we chose another target using the same procedure above to do the tracking and signature extraction. The results are shown in figures below.

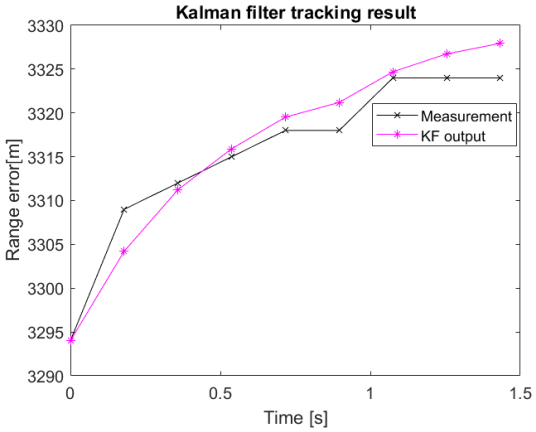

Figure 5.14: Filter output of target 2

The tracking offset compared to the measurements at each time step can be seen in figure 5.15.

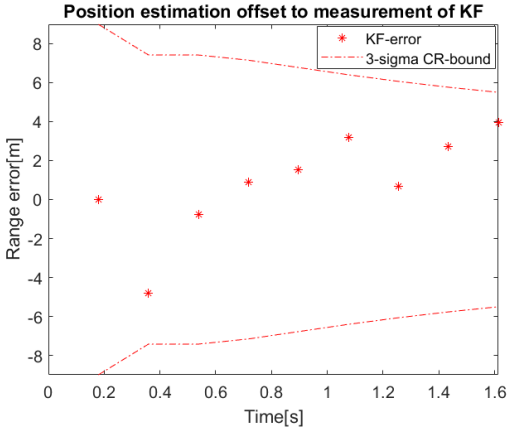

Figure 5.15: Tracking offset of target 2

As we can see in figure 5.14 and figure 5.15, the trajectory of the target has been smoothed after tracking. The error is more significant than that for target one because

the target is accelerating (it is not moving with constant velocity in the observed interval). However, it is still acceptable in this case.

The signature of the target is extracted in figure 5.16.

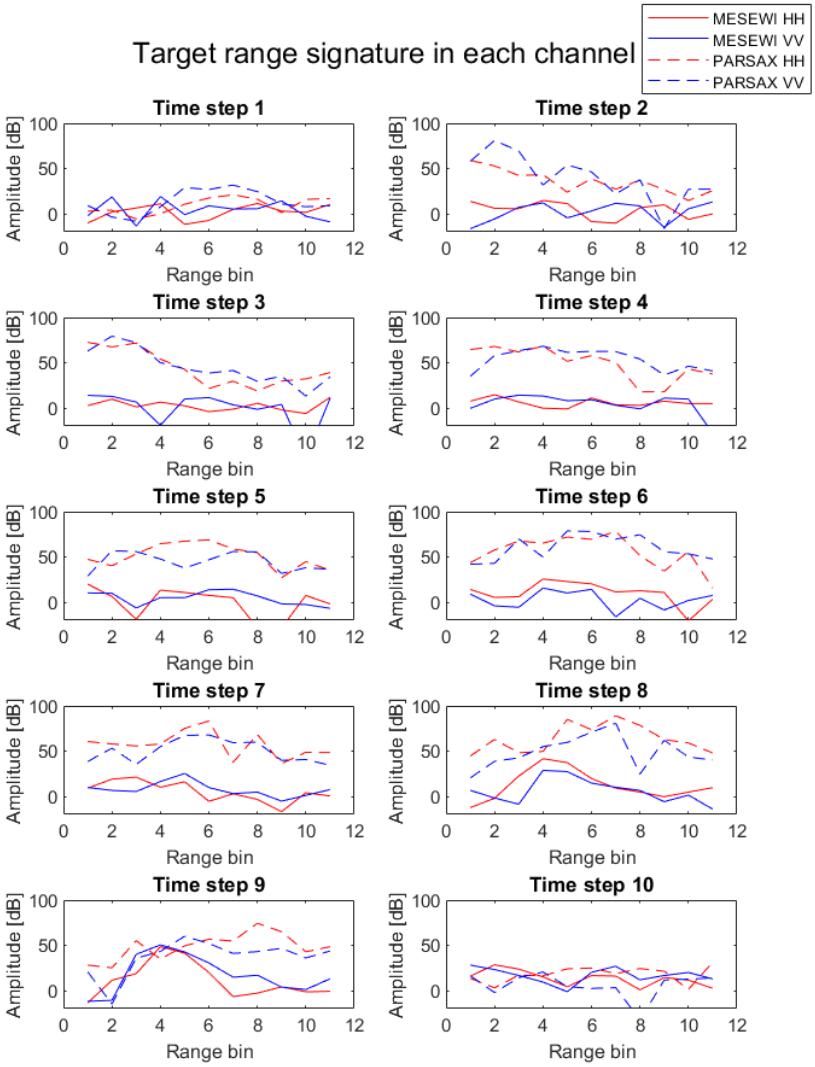

Figure 5.16: Range signature of target 2(real data)

We can see that the target in PARSAX has around 30dB higher SNR than MESEWI, and its signature varies across polarimetric channels. Notice that the two radars have

different transmit power, antenna gain, and noise floor; therefore, the presented curves can be compared between radars only in terms of their shapes. In order to compare them in terms of RCS, both radars should be appropriately calibrated (in power), and their data sets should be normalized accordingly. Such calibration can be done using a target with high and stable RCS, e.g., a trihedral corner reflector.

5.6. CONCLUSION

In this chapter, the output of the logic rule in chapter 4 was used as the measurement of range and velocity. Kalman filter was used based on these measurements to do the single target tracking. Kalman filter result demonstrated that the proposed method could give a slight position estimation error in numerical simulation. Application of the algorithm developed to the experimental data from PARSAX and MESEWI radars has been done. It is shown that a single target can be tracked successfully using the output from the data fusion rule for the actual data. A method of target range signature extraction was proposed and analyzed. We conclude that the two radars' joint processing procedure is feasible and could be used for single target tracking and target signature extraction. The range signature can be used for target classification.

6

CONCLUSIONS AND FUTURE WORK

6.1. CONCLUSIONS

In this project, the joint processing of two radars located on the rooftop of the EWI building, namely PARSAX, and MESEWI, has been investigated. The alignment procedure for data from both radars has been developed and experimentally verified. The multi-channel detection algorithms and procedures for target responses extraction have been investigated. In more detail, the major contributions of the thesis can be summarized as follows.

- The cross-correlation method has been applied to the spatial alignment of two independent radars' data and tested with numerical simulation and actual data. The simulation result proves the feasibility of two independent radars' alignment in space and indicates that the method's accuracy is satisfactory. Tested with SSIM value at each processing step, data with higher range and angle resolution and a wider antenna's beamwidth could give a better result after the spatial alignment procedure. The estimated cable length of PARSAX for actual data is around 36.8m, and the position displacement of the two radars is 2.3m and -9.1m in latitude and meridian direction, respectively. The SSIM value increases after each processing step as expected. The results agree well with the actual geometry of radars installation on the rooftop of EWI.
- Temporal alignment was done using cross-correlation on the slow-time data. The impact of several parameters on the estimation error was analyzed. Higher SNR, resolution, and relatively longer processing time would give a minor estimation error based on MSE evaluation. Furthermore, the experimental validation demonstrates that the time offset estimation of the two radars is around 0.89s. After data alignment in spatial and temporal domains, the targets coincide on the range-slow-time and range-Doppler plots.
- Two rules of fusing the radar data from different radars and polarized channels have been proposed and tested with simulation. The simulation result shows that

data fusion of different polarized channels improves radar performance in the probability of detection for weak targets by increasing the target response's total amplitude. Different frequency data fusion resolves the velocity ambiguity that appeared in a single radar, improves performance in the probability of target detection, and improves the probability of correct estimations of the target range and velocity. By comparing the results, the proposed logic, which requires the target to be detected in at least one radar channel of each radar, is a suitable way to do the data fusion from different radars and channels.

- Target tracking was implemented based on the aligned data using Kalman filter, and a method to extract the target's signatures was developed. This procedure was verified by means of numerical simulation and validated on actual data. In simulations, the multi-channel data was well-aligned, and the tracking result was close to the actual trajectory with a slight position estimation error. Application of the method developed to the experimental data has demonstrated that a single target is tracked successfully using the output from the data fusion rule. The ambiguity of velocity appearing in a single radar measurement is also resolved.

- Range signatures of a few targets have been extracted. The measured signatures of the targets can be further used for targets' classification.

The results listed above prove that the two radars' joint processing procedure is feasible and that the algorithms developed are helpful for a single target tracking. The practical importance of the procedures and algorithms developed lies in the possibility of extracting multi-polarization multi-frequency target responses, which are essential for unambiguous target classification.

6.2. FUTURE WORK

The work performed can be further extended in the following directions.

- Multiple target tracking using Multi Target Data Association filter (MTDF) [33].

- Multiple target feature extraction and classification could be done with some data association methods.

- Other methods for the data fusion part can be used, like applying some detectors which can use some mathematical approach to fuse the data from different polarized channels.

BIBLIOGRAPHY

[1] Renuka Anitha, S Renuka, and A Abudhahir. "Multi sensor data fusion algorithms for target tracking using multiple measurements". In: *2013 IEEE International Conference on Computational Intelligence and Computing Research*. IEEE. 2013, pp. 1–4.

[2] Paul E. Anuta. "Spatial Registration of Multispectral and Multitemporal Digital Imagery Using Fast Fourier Transform Techniques". In: *IEEE Transactions on Geoscience Electronics* 8.4 (1970), pp. 353–368. DOI: 10.1109/TGE.1970.271435.

[3] David Arthur and Sergei Vassilvitskii. *k-means++: The advantages of careful seeding*. Tech. rep. Stanford, 2006.

[4] Yaakov Bar-Shalom and Edison Tse. "Tracking in a cluttered environment with probabilistic data association". In: *Automatica* 11.5 (1975), pp. 451–460.

[5] Stéphanie Bidon, Laurent Savy, and François Deudon. "Fast coherent integration for migrating targets with velocity ambiguity". In: *2011 IEEE RadarCon (RADAR)*. IEEE. 2011, pp. 027–032.

[6] W-M Boerner, AB Kostinski, and BD James. "On the concept of the polarimetric matched filter in high resolution radar imaging: An alternative for speckle radiation". In: *Remote Sensing: Moving Towards the 21st Century* 1 (1988), pp. 69–72.

[7] XUE Cewen et al. "Multi-polarization Data Fusion Analysis of Full-Polarimetric Ground Penetrating Radar". In: 10.1 (2021), pp. 74–85.

[8] YT Chan, AGC Hu, and JB Plant. "A Kalman filter based tracking scheme with input estimation". In: *IEEE transactions on Aerospace and Electronic Systems* 2 (1979), pp. 237–244.

[9] RD Chaney, MC Bud, and LM Novak. "On the performance of polarimetric target detection algorithms". In: *IEEE Aerospace and Electronic Systems Magazine* 5.11 (1990), pp. 10–15.

[10] I-S Choi et al. "Radar target recognition using one-dimensional evolutionary programming–based CLEAN". In: *Journal of Electromagnetic Waves and Applications* 17.5 (2003), pp. 763–784.

[11] SR DeGraaf. "SAR image enhancement via adaptive polarization synthesis and polarimetric detection performance". In: *Proc. Polarimetric Technol. Workshop*. Vol. 1. Redstone Arsenal. 1988, p. 1.

[12] Francesca Filippini and Fabiola Colone. "Polarimetric passive radar: a practical approach to parametric adaptive detection". In: *IEEE Transactions on Aerospace and Electronic Systems* 56.6 (2020), pp. 4930–4946.

[13] Qiang Gan and Chris J Harris. “Comparison of two measurement fusion methods for Kalman-filter-based multisensor data fusion”. In: *IEEE Transactions on Aerospace and Electronic systems* 37.1 (2001), pp. 273–279.

[14] Simon Haykin et al. *Remote sensing of sea ice and icebergs*. Vol. 13. John Wiley & Sons, 1994.

[15] Eric Jacobsen and Peter Kootsookos. “Fast, accurate frequency estimators [DSP Tips & Tricks]”. In: *IEEE Signal Processing Magazine* 24.3 (2007), pp. 123–125.

[16] Wang Juanjuan and Huang Jianjun. “A spatial alignment algorithm for time varying biases of radar and infrared sensors”. In: *Procedia Engineering* 15 (2011). CEIS 2011, pp. 2614–2618. ISSN: 1877-7058. DOI: https://doi.org/10.1016/j.proeng.2011.08.491. URL: https://www.sciencedirect.com/science/article/pii/S1877705811019928.

[17] TERRENCE J Keating, PR Wolf, and FL Scarpace. “An improved method of digital image correlation”. In: *Photogrammetric Engineering and Remote Sensing* 41.8 (1975), pp. 993–1002.

[18] Bahador Khaleghi et al. “Multisensor data fusion: A review of the state-of-the-art”. In: *Information fusion* 14.1 (2013), pp. 28–44.

[19] K-T Kim and HT Kim. “One-dimensional scattering centre extraction for efficient radar target classification”. In: *IEE Proceedings-Radar, Sonar and Navigation* 146.3 (1999), pp. 147–158.

[20] Thia Kirubarajan et al. “Ground target tracking with variable structure IMM estimator”. In: *IEEE Transactions on Aerospace and Electronic Systems* 36.1 (2000), pp. 26–46.

[21] Oleg A Krasnov et al. “The PARSAX-full polarimetric FMCW radar with dual-orthogonal signals”. In: *2008 European Radar Conference*. IEEE. 2008, pp. 84–87.

[22] Chevalier François Le. *Principles of radar and sonar signal processing*. Artech House, 2002.

[23] Seung-Jae Lee, In-Sik Choi, and Dae-Young Chae. “A novel feature extraction method for radar target classification using fusion of early-time and late-time regions”. In: *Journal of ElEctromagnEtic WavEs and applications* 31.10 (2017), pp. 1020–1033.

[24] Xian-ming LIU, Kai XIE, and Xue-wu WU. “A new method of eliminating high-speed target s velocity ambiguity in LFMCW radar”. In: *Modern Electronics Technique* 7 (2012).

[25] Ari Löytynoja and Michel C. Milinkovitch. “A hidden Markov model for progressive multiple alignment”. In: *Bioinformatics* 19.12 (Aug. 2003), pp. 1505–1513. ISSN: 1367-4803. DOI: 10.1093/bioinformatics/btg193. eprint: https://academic.oup.com/bioinformatics/article-pdf/19/12/1505/717058/btg193.pdf. URL: https://doi.org/10.1093/bioinformatics/btg193.

[26] Guoze Lu et al. “Multi-frequency and multi-attribute GPR data fusion based on 2-D wavelet transform”. In: *Measurement* 166 (2020), p. 108243.

[27] H Lu and PD Cary. “Deformation measurements by digital image correlation: implementation of a second-order displacement gradient”. In: *Experimental mechanics* 40.4 (2000), pp. 393–400.

[28] Samaneh Mazaheri et al. “Hybrid pixel-based method for cardiac ultrasound fusion based on integration of PCA and DWT”. In: *Computational and mathematical methods in medicine* 2015 (2015).

[29] Daniel McDuff et al. “Affect valence inference from facial action unit spectrograms”. In: *2010 IEEE Computer Society Conference on Computer Vision and Pattern Recognition - Workshops*. 2010, pp. 17–24. DOI: 10.1109/CVPRW.2010.5543833.

[30] K Rajalakshmi Menon, N Balakrishnan, and K Ramchand. “Discriminating complex bodies with minor variations using e-pulse”. In: *IEEE Transactions on Aerospace and Electronic Systems* 44.1 (2008), pp. 408–416.

[31] *Microwave Sensing, Signals and Systems–Main Characteristics of the PARSAX Radar*. http://radar.ewi.tudelft.nl/Facilities/parsax_spec.php.

[32] Shyam Mohan M et al. “Introduction to the Kalman filter and tuning its statistics for near optimal estimates and Cramer Rao bound”. In: *arXiv e-prints* (2015), arXiv–1503.

[33] Saravanan Nagesh. “Robust Feature Extraction Algorithm for analysis of Radar Targets using Multi-Object Tracking on Range Velocity Space”. In: (2019).

[34] Leslie M Novak and Michael C Burl. “Optimal speckle reduction in polarimetric SAR imagery”. In: *Twenty-Second Asilomar Conference on Signals, Systems and Computers*. Vol. 2. IEEE. 1988, pp. 781–793.

[35] Leslie M Novak, Michael B Sechtin, and Michele J Cardullo. “Studies of target detection algorithms that use polarimetric radar data”. In: *IEEE Transactions on Aerospace and Electronic Systems* 25.2 (1989), pp. 150–165.

[36] Kenji Okuma et al. “A boosted particle filter: Multitarget detection and tracking”. In: *European conference on computer vision*. Springer. 2004, pp. 28–39.

[37] N. Petrov. “Migrating Target Detection in Wideband Radars”. PhD thesis. Delft University of Technology, 2019.

[38] Nikita Petrov and Francois Le Chevalier. “Fast implementation of iterative adaptive approach for wideband unambiguous radar detection”. In: *2015 23rd European Signal Processing Conference (EUSIPCO)*. IEEE. 2015, pp. 1207–1211.

[39] Hossein Pishro-Nik. “Introduction to probability, statistics, and random processes”. In: (2016).

[40] Chotirat Ratanamahatana and Eamonn Keogh. “Three Myths about Dynamic Time Warping Data Mining”. In: Apr. 2005. DOI: 10.1137/1.9781611972757.50.

[41] Matthew Rhudy. “Time alignment techniques for experimental sensor data”. In: *International Journal of Computer Science and Engineering Survey* 5.2 (2014), p. 1.

[42] Mark A Richards. *Fundamentals of radar signal processing*. McGraw-Hill Education, 2014.

[43] Edward Rothwell et al. “Radar target discrimination using the extinction-pulse technique”. In: *IEEE Transactions on Antennas and Propagation* 33.9 (1985), pp. 929–937.

[44] Kenshi Saho. “Kalman filter for moving object tracking: Performance analysis and filter design”. In: *Kalman Filters-Theory for Advanced Applications* (2017), pp. 233–252.

[45] Sharada C. Sajjan and C Vijaya. “Comparison of DTW and HMM for isolated word recognition”. In: *International Conference on Pattern Recognition, Informatics and Medical Engineering (PRIME-2012)*. 2012, pp. 466–470. DOI: 10.1109/ICPRIME.2012.6208391.

[46] Ashbindu Singh and Andrew Harrison. “Standardized principal components”. In: *International journal of remote sensing* 6.6 (1985), pp. 883–896.

[47] Zhou Wang et al. “Image quality assessment: from error visibility to structural similarity”. In: *IEEE transactions on image processing* 13.4 (2004), pp. 600–612.

[48] Jiapeng Yin, Christine MH Unal, and Herman WJ Russchenberg. “Narrow-band clutter mitigation in spectral polarimetric weather radar”. In: *IEEE Transactions on Geoscience and Remote Sensing* 55.8 (2017), pp. 4655–4667.

[49] NH Younan. “Radar target identification via a combined E-pulse/SVD-Prony method”. In: *Record of the IEEE 2000 International Radar Conference [Cat. No. 00CH37037]*. IEEE. 2000, pp. 799–803.

[50] Zhihua Yuan et al. “Solving Velocity Ambiguity for Pulse Doppler Radar Space Target Measurement”. In: *IOP Conference Series: Materials Science and Engineering*. Vol. 608. 1. IOP Publishing. 2019, p. 012038.

[51] Song Yuegang and An Hong. “A New Algorithm for Range and Velocity Ambiguity Resolution at Medium PRF [J]”. In: *Fire Control Radar Technology* 1 (2009).

[52] Yifeng Zhou, Henry Leung, and Patrick C Yip. “An exact maximum likelihood registration algorithm for data fusion”. In: *IEEE Transactions on Signal Processing* 45.6 (1997), pp. 1560–1573.